

# Full-Folding Optical Potentials for Elastic Nucleon-Nucleus Scattering based on Realistic Densities

Ch. Elster, S.P. Weppner

*Institute of Nuclear and Particle Physics, and Department of Physics,  
Ohio University, Athens, OH 45701*

C.R. Chinn \*

*Department of Physics and Astronomy, Vanderbilt University, Nashville, TN 37235  
(February 9, 2008)*

## Abstract

Optical model potentials for elastic nucleon nucleus scattering are calculated for a number of target nuclides from a full-folding integral of two different realistic target density matrices together with full off-shell nucleon-nucleon t-matrices derived from two different Bonn meson exchange models. Elastic proton and neutron scattering observables calculated from these full-folding optical potentials are compared to those obtained from ‘optimum factorized’ approximations in the energy regime between 65 and 400 MeV projectile energy. The optimum factorized form is found to provide a good approximation to elastic scattering observables obtained from the full-folding optical potentials, although the potentials differ somewhat in the structure of their nonlocality.

PACS: 25.40.Cm, 25.40Dn, 24.10.Ht

Typeset using REVTeX

---

\*present address: Areté Associates, P.O. Box 16269, Arlington, VA 22215

## I. INTRODUCTION

Progress in the rigorous treatment of the multiple scattering of nucleons from nuclei has led to the need to study the influence of the full target nuclear density matrix in the scattering observables. In first order the spectator expansion of multiple scattering theory requires a convolution of the fully off-shell nucleon-nucleon (NN) scattering amplitude with the nuclear wave functions of the target. This opens the possibility to assess the influence of the target wave functions on elastic proton and neutron scattering observables.

In its most general form, the first order single scattering optical potential within the framework of the spectator expansion is given by the triangle graph shown in Fig. 1. Since there is one loop, the evaluation of the graph requires a three-dimensional integration involving the fully-off-shell two-nucleon scattering amplitude and a realistic nuclear density matrix. Usually, one makes the assumption that the NN amplitude varies slowly as a function of its arguments compared to the nuclear density matrix. This corresponds to the argument that the range of the NN force is small compared to the size of the nucleus and leads to the approximate nonrelativistic form  $t(q)\rho(q)$  for the first-order nucleon-nucleus optical potential. Full-folding calculations, avoiding this approximation, have already been performed by several groups based on either the KMT approach [2,3] or a g-matrix approach [4,5] using various models for the off-shell density matrix as well as different models for the NN amplitudes. In general, this work indicates that an improved treatment of the off-shell structure of the optical potential improves the description of the observables.

Our approach to elastic scattering from nuclei is based on the spectator expansion of multiple scattering theory [6–8]. Here the first order term involves two-body interactions between the projectile and one of the target nucleons. Due to the many-body nature of the free propagator for the projectile+target nucleon system, a theoretical treatment of this many-body propagator as affected by the residual target nucleus is included. The calculation of the optical potential presented in this paper relies on two basic inputs. One is the fully off-shell NN t-matrix, which represents the current understanding of the nuclear force, and the other is the nuclear wave function of the target, representing the best understanding of the ground state of the target nucleus. To account for the modifications of the free propagator inside the nucleus, the same mean field potentials are used from which the ground state wave functions are derived. There are *no* adjustable parameters present in this calculation.

The motivation for ongoing work on this topic is twofold. First, elastic and inelastic nucleon-nucleus scattering provide an important and sensitive test for theoretical corrections at the first-order level of the optical potential (*e.g.* as given by possibly genuine modifications of the NN interaction in the nuclear environment and off-shell effects). Rigorous microscopic calculations are required for discerning these effects. Second, a better understanding of the theoretical details of the optical potential are needed to construct realistic and physically sound wave functions representing continuum nucleons in the interior of the nucleus. These wave functions will become vital for future theoretical needs in high-energy coincidence experiments (at TJNAF *e.g.*), inelastic scattering studies, and for understanding the reactions in heavy ion experiments involving nuclei far from the drip lines. Here experiments involving the scattering of exotic nuclei from single nucleon targets should benefit from full-folding type calculations in order to test the predicted density distributions of halo-like nuclei.

The structure of the paper is as follows. In Section II we review the relevant formalism for the single-scattering optical potential and introduce the full-folding procedure as used in our calculations. In Section III we discuss the model densities employed and describe the calculations of the full folding optical potentials. Elastic scattering results for neutron and proton scattering from a variety of nuclei in the energy regime between 65 and 400 MeV are discussed in Section IV. Our conclusions are presented in Section V.

## II. THE FULL-FOLDING OPTICAL POTENTIAL

The standard approach to elastic scattering of a strongly interacting projectile from a target of  $A$  particles is the separation of the Lippmann-Schwinger equation for the transition amplitude

$$T = V + VG_0(E)T \quad (2.1)$$

into two parts, namely an integral equation for  $T$ :

$$T = U + UG_0(E)PT, \quad (2.2)$$

where  $U$  is the optical potential operator and defined by a second integral equation

$$U = V + VG_0(E)QU. \quad (2.3)$$

In the above equations the operator  $V$  represents the external interactions between the projectile and the target nucleons. Therefore the Hamiltonian for the  $(A + 1)$  particle system is given by

$$H = H_0 + V. \quad (2.4)$$

The free propagator  $G_0(E)$  for the projectile-target system is given by

$$G_0(E) = (E - H_0 + i\epsilon)^{-1}. \quad (2.5)$$

The potential operator  $V = \sum_{i=1}^A v_{0i}$  consists of the two-body potential  $v_{0i}$  acting between the projectile and the  $i$ th target nucleon. The operators  $P$  and  $Q$  are projection operators,  $P + Q = 1$ , and  $P$  is defined such that Eq. (2.2) is solvable. In this case,  $P$  is conventionally taken to project onto the elastic channel, such that  $[G_0, P] = 0$ . The free Hamiltonian is given by

$$H_0 = h_0 + H_A \quad (2.6)$$

where  $h_0$  is the kinetic energy operator for the projectile and  $H_A$  stands for the target Hamiltonian. Thus the projector  $P$  can be defined as

$$P = \frac{|\Phi_A\rangle\langle\Phi_A|}{\langle\Phi_A|\Phi_A\rangle} \quad (2.7)$$

where  $|\Phi_A\rangle$  corresponds to the ground state of the target and fulfills

$$H_A|\Phi_A\rangle = E_A|\Phi_A\rangle \quad (2.8)$$

With these definitions the transition operator for elastic scattering can be defined as  $T_{el} = PTP$ , in which case Eqs. (2.2) becomes

$$T_{el} = PUP + PUPG_0(E)T_{el}. \quad (2.9)$$

The fundamental idea of the spectator expansion for the optical potential is an ordering of the scattering process according to the number of active target nucleons interacting directly with the projectile. The first order term involves two-body interactions between the projectile and one of the target nucleons, i.e.

$$U = \sum_{i=1}^A \tau_i, \quad (2.10)$$

where the operator  $\tau_i$  is derived to be

$$\begin{aligned} \tau_i &= v_{0i} + v_{0i}G_0(E)Q\tau_i \\ &= v_{0i} + v_{0i}G_0(E)\tau_i - v_{0i}G_0(E)P\tau_i \\ &= \hat{\tau}_i - \hat{\tau}_iG_0(E)P\tau_i. \end{aligned} \quad (2.11)$$

For elastic scattering only  $P\tau_iP$ , or equivalently  $\langle\Phi_A|\tau_i|\Phi_A\rangle$  need to be considered,

$$\langle\Phi_A|\tau_i|\Phi_A\rangle = \langle\Phi_A|\hat{\tau}_i|\Phi_A\rangle - \langle\Phi_A|\hat{\tau}_i|\Phi_A\rangle \frac{1}{(E - E_A) - h_0 + i\varepsilon} \langle\Phi_A|\tau_i|\Phi_A\rangle, \quad (2.12)$$

where  $\hat{\tau}_i$  is defined as the solution of

$$\hat{\tau}_i = v_{0i} + v_{0i}G_0(E)\hat{\tau}_i. \quad (2.13)$$

It should be noted that Eqs. (2.3) to (2.13) all follow in a straightforward derivation and correspond to the first order Watson scattering expansion [9]. If the projectile – target nucleon interaction is assumed to be the same for all target nucleons and if isospin effects are neglected then the KMT scattering integral equation [10] can be directly derived from the first order Watson scattering expansion.

Since Eq. (2.12) is a simple one-body integral equation, the principal problem is to find a solution of Eq. (2.13), which has a many-body character due to  $G_0(E) = (E - h_0 - H_A + i\varepsilon)^{-1}$ . If the propagator  $G_0(E)$  is expanded in the spirit of the spectator expansion within a single particle description, one obtains in first order [1,11]

$$G_i(E) = [(E - E^i) - h_0 - h_i - W_i + i\varepsilon]^{-1}, \quad (2.14)$$

where  $h_i$  is the kinetic energy of the  $i$ th target particle and  $W_i = \sum_{j \neq i} v_{ij}$ . The quantity  $W_i$  represents the force acting between the struck target nucleon and the residual (A-1) nucleus. Then the operator  $\hat{\tau}_i$  of Eq.(2.13) can be written as

$$\begin{aligned} \hat{\tau}_i &= v_{0i} + v_{0i}G_i(E)\hat{\tau}_i \\ &= t_{0i} + t_{0i}g_iW_iG_i(E)\hat{\tau}_i. \end{aligned} \quad (2.15)$$

Here the operators  $t_{0i}$  and  $g_i$  are defined as

$$t_{0i} = v_{0i} + v_{0i}g_it_{0i} \quad (2.16)$$

and

$$g_i = [(E - E^i) - h_0 - h_i + i\varepsilon]^{-1}. \quad (2.17)$$

The operator  $t_{0i}$  can be identified with the free NN t-matrix, and in lowest order the operator  $\hat{\tau}_i$  of Eq. (2.15) is given by  $\hat{\tau}_i \approx t_{0i}$ . From now on we consider for clarity in presentation only this case.

The matrix element  $\langle \Phi_A | \tau_i | \Phi_A \rangle$  given in Eq. (2.12) represents the full-folding optical potential and is given explicitly as

$$\langle \mathbf{k}' | U | \mathbf{k} \rangle = \langle \mathbf{k}' \Phi_A | \sum_{\alpha=p,n} \tau_\alpha | \mathbf{k} \Phi_A \rangle, \quad (2.18)$$

where  $\alpha$  represents the sum over the target protons and neutrons. Since  $\langle \mathbf{k}' | U | \mathbf{k} \rangle$  is the solution of the sum of the one-body integral equations represented by Eq. (2.12), it is sufficient to consider the driving term

$$\langle \mathbf{k}' | \hat{U} | \mathbf{k} \rangle = \langle \mathbf{k}' \Phi_A | \sum_{\alpha=p,n} \hat{\tau}_\alpha | \mathbf{k} \Phi_A \rangle, \quad (2.19)$$

where  $\hat{\tau}_\alpha$  is given by Eq. (2.13).

Inserting a complete set of momenta for the struck target nucleon before and after the collision Eq. (2.19) reads

$$\hat{U}(\mathbf{k}, \mathbf{k}') = \sum_{\alpha=p,n} \int d^3\mathbf{p}' d^3\mathbf{p} \langle \mathbf{k}' \mathbf{p}' | \hat{\tau}_\alpha(\epsilon) | \mathbf{k} \mathbf{p} \rangle \rho_\alpha \left( \mathbf{p}' + \frac{\mathbf{k}'}{A}, \mathbf{p} + \frac{\mathbf{k}}{A} \right) \delta^3(\mathbf{k}' + \mathbf{p}' - \mathbf{k} - \mathbf{p}). \quad (2.20)$$

The momenta  $\mathbf{k}'$  and  $\mathbf{k}$  are the final and initial momenta of the projectile in the frame of zero total nucleon-nucleus momentum. The structure of Eq. (2.20) is represented graphically by Fig 1, which also illustrates the momenta  $\mathbf{p}'$  and  $\mathbf{p}$ . The proton and neutron density matrices are given by  $\rho_\alpha$ . By evaluating the  $\delta$ -function and introducing the variables  $\mathbf{q} = \mathbf{k}' - \mathbf{k}$ ,  $\mathbf{K} = \frac{1}{2}(\mathbf{k} + \mathbf{k}')$  and  $\hat{\mathbf{p}} = \frac{1}{2}(\mathbf{p}' + \mathbf{p})$  we obtain

$$\begin{aligned} \hat{U}(\mathbf{q}, \mathbf{K}) = \sum_{\alpha=p,n} \int d^3\hat{\mathbf{p}} \left\langle \mathbf{k}', \hat{\mathbf{p}} - \frac{1}{2}\mathbf{q} \middle| \hat{\tau}_\alpha(\epsilon) \middle| \mathbf{k}, \hat{\mathbf{p}} + \frac{1}{2}\mathbf{q} \right\rangle \\ \rho_\alpha \left( \hat{\mathbf{p}} - \frac{A-1}{A}\frac{\mathbf{q}}{2} + \frac{\mathbf{K}}{A}, \hat{\mathbf{p}} + \frac{A-1}{A}\frac{\mathbf{q}}{2} + \frac{\mathbf{K}}{A} \right). \end{aligned} \quad (2.21)$$

A change of the integration variable from  $\hat{\mathbf{p}}$  to  $\mathbf{P} = \hat{\mathbf{p}} + \frac{\mathbf{K}}{A}$ , accounting for the recoil of the nucleus, gives [13]

$$\begin{aligned} \hat{U}(\mathbf{q}, \mathbf{K}) = \sum_{\alpha=p,n} \int d^3\mathbf{P} \left\langle \mathbf{k}', \mathbf{P} - \frac{\mathbf{q}}{2} - \frac{\mathbf{K}}{A} \middle| \hat{\tau}_\alpha(\epsilon) \middle| \mathbf{k}, \mathbf{P} + \frac{\mathbf{q}}{2} - \frac{\mathbf{K}}{A} \right\rangle \\ \rho_\alpha \left( \mathbf{P} - \frac{A-1}{A}\frac{\mathbf{q}}{2}, \mathbf{P} + \frac{A-1}{A}\frac{\mathbf{q}}{2} \right). \end{aligned} \quad (2.22)$$

The NN amplitude  $\hat{\tau}_\alpha$  in Eq. (2.22) is evaluated in the zero momentum frame of the nucleon-nucleus system. The relationship to the corresponding matrix element evaluated in the zero momentum frame of the two nucleons is given by

$$\left\langle \mathbf{k}', \mathbf{P} - \frac{\mathbf{q}}{2} - \frac{\mathbf{K}}{A} \mid \hat{\tau}_\alpha(\epsilon) \mid \mathbf{k}, \mathbf{P} + \frac{\mathbf{q}}{2} - \frac{\mathbf{K}}{A} \right\rangle_{NA} = \eta(\mathbf{P}, \mathbf{q}, \mathbf{K}) \langle \mathcal{K}', -\mathcal{K}' \mid \hat{\tau}_\alpha(\epsilon) \mid \mathcal{K}, -\mathcal{K} \rangle_{NN}, \quad (2.23)$$

where  $\mathcal{K}' = \frac{1}{2}(\mathbf{k}' - (\mathbf{P} - \frac{\mathbf{q}}{2} - \frac{\mathbf{K}}{A}))$  and  $\mathcal{K} = \frac{1}{2}(\mathbf{k} - (\mathbf{P} + \frac{\mathbf{q}}{2} - \frac{\mathbf{K}}{A}))$  are the nonrelativistic final and initial nuclear momenta in the zero momentum frame of the NN system. The factor  $\eta(\mathbf{P}, \mathbf{q}, \mathbf{K})$  is the Møller factor for the frame transformation [14] and is given by

$$\eta(\mathbf{P}, \mathbf{q}, \mathbf{K}) = \left[ \frac{E_N(\mathcal{K}')E_N(-\mathcal{K}')E_N(\mathcal{K})E_N(-\mathcal{K})}{E_N(k')E_N(\mathbf{P} - \frac{\mathbf{q}}{2} - \frac{\mathbf{K}}{A})E_N(k)E_N(\mathbf{P} + \frac{\mathbf{q}}{2} - \frac{\mathbf{K}}{A})} \right], \quad (2.24)$$

where  $E_N(\mathbf{k})$  is the relativistic kinetic energy of a nucleon of momentum  $k$ . This factor imposes the Lorentz invariance of the flux. With this frame transformation taken into account, the full-folding optical potential of Eq. (2.22) can be written as

$$\begin{aligned} \hat{U}(\mathbf{q}, \mathbf{K}) = \sum_{\alpha=p,n} \int d^3\mathbf{P} \, \eta(\mathbf{P}, \mathbf{q}, \mathbf{K}) \, \hat{\tau}_\alpha \left( \mathbf{q}, \frac{1}{2} \left( \frac{A+1}{A} \mathbf{K} - \mathbf{P} \right); \epsilon \right) \\ \rho_\alpha \left( \mathbf{P} - \frac{A-1}{A} \frac{\mathbf{q}}{2}, \mathbf{P} + \frac{A-1}{A} \frac{\mathbf{q}}{2} \right). \end{aligned} \quad (2.25)$$

Here the arguments of  $\hat{\tau}_\alpha$  are  $\mathbf{q} = \mathbf{k}' - \mathbf{k} = \mathcal{K}' - \mathcal{K}$  and  $\frac{1}{2}(\mathcal{K}' + \mathcal{K}) = \frac{1}{2}(\frac{A+1}{A}\mathbf{K} - \mathbf{P})$ .

The two-nucleon amplitude  $\hat{\tau}_\alpha$  is calculated from the free NN t-matrix according to Eqs. (2.15) and (2.16) at an appropriate energy  $\epsilon$ . In principle, this energy should be the beam energy minus the kinetic energy of the center of mass of the interacting pair less the binding energy of the struck particle. Following this argument,  $\epsilon$  should be coupled to the integration variable  $\mathbf{P}$ . The full-folding calculations of Refs. [4,5] are carried out along this vain. For our calculations we take a different approach, namely we fix  $\epsilon$  at the two-body center-of-mass (c.m.) energy corresponding to free NN scattering at the beam energy so that the same laboratory energy applies to the two-body and nuclear scattering. This approach has been applied in earlier work [3] and is also used in the work of the Surrey Group [2].

### III. MODELS FOR THE OFF-SHELL DENSITY

The evaluation of the full-folding optical potential as given in Eq. (2.25) requires a nuclear density matrix, which in a single particle picture is given as

$$\rho_\alpha(\tilde{\mathbf{p}}', \tilde{\mathbf{p}}) = \sum_i \Psi_{\alpha,i}^\dagger(\tilde{\mathbf{p}}') \Psi_{\alpha,i}(\tilde{\mathbf{p}}) \quad (3.1)$$

Here  $\Psi_{\alpha,i}(\tilde{\mathbf{p}})$  are the wave functions describing the single particle nuclear ground state. The index  $\alpha$  stands for protons and neutrons, respectively, and the total nuclear ground state is given by the sum of the two. In order to achieve consistency with our formulation of incorporating effects of the ‘nuclear medium’ on the scattering process we choose as model density matrices the ones from which the nuclear mean fields  $W_i$  are derived (see e.g. Eq. (2.15)).

The models used are a non-relativistic reduction of a Dirac-Hartree calculation [16] and a non-relativistic Hartree-Fock-Bogolyubov (HFB) structure calculation [17,18]. The Dirac-Hartree calculation is a spherical solution of the one-body Dirac equation assuming a scalar potential and the time component of a vector potential field. The nonrelativistic HFB microscopic nuclear structure calculation uses the parameterized effective finite-range, density dependent Gogny D1S effective NN interaction. The parameter of the Gogny D1S interaction are fitted to a certain set of stable nuclei. For this case an axial harmonic oscillator basis is used.

The details of the Dirac-Hartree (DH) calculation leading to the density matrices employed in our calculations are given below. The wave function  $\Psi_i(\mathbf{r})$  is a solution of the one-body Dirac-Hartree equation and given by [19]

$$\Psi_\beta(\mathbf{r}) \equiv \Psi_{n,\nu,m,t_z}(\mathbf{r}) = \begin{pmatrix} i \left[ \frac{G_{t_z,n,\nu}(r)}{r} \right] \phi_{\nu m} \\ - \left[ \frac{F_{t_z,n,\nu}(r)}{r} \right] \phi_{-\nu m} \end{pmatrix} \zeta_{t_z} \quad (3.2)$$

Here  $t_z$  stands for the z component of the isospin and  $n$  for the principal quantum number. The phase convention is taken from Ref. [19]. During this derivation we prefer to omit the index  $\alpha$ . The spherical harmonics are determined by  $\phi_{\nu m}$  which is defined as

$$\phi_{\nu m} = \sum_{m_l, m_s} \langle l m_l \frac{1}{2} m_s | l \frac{1}{2} j m \rangle Y_l^{m_l}(\Omega) \chi_{m_s}, \quad (3.3)$$

where  $Y_l^{m_l}(\Omega)$  is a spherical harmonic and  $\chi_{m_s}$  a Pauli spinor. The quantum number  $\nu$  uniquely defines  $j$  and  $l$  as

$$j = |\nu| - \frac{1}{2}, \quad l = \begin{cases} \nu, & \nu > 0 \\ -(\nu + 1), & \nu < 0 \end{cases}. \quad (3.4)$$

We used the code *Timora* [19] and the parameter sets given therein to generate the functions  $G$  and  $F$  given in Eq.(3.2) for the nuclei studied in this paper.

Under the assumption of orthogonal single particle states the density matrix is given in coordinate space by

$$\begin{aligned} \rho(\mathbf{r}', \mathbf{r}) &= \sum_{n\nu m} \Psi_{n\nu m t_z}^\dagger(\mathbf{r}') \Psi_{n\nu m t_z}(\mathbf{r}) \\ &= \sum_{n\nu} \left[ \frac{G_{t_z,n,\nu}(r')}{r'} \frac{G_{t_z,n,\nu}(r)}{r} \sum_m \phi_{\nu m}(r') \phi_{\nu m}(r) + \frac{F_{t_z,n,\nu}(r')}{r'} \frac{F_{t_z,n,\nu}(r)}{r} \sum_m \phi_{-\nu m}(r') \phi_{-\nu m}(r) \right]. \end{aligned} \quad (3.5)$$

Here we should point out that in order to obtain a density matrix which we can apply in our formulation of the optical potential, we have a  $\mathbf{1}$ -operator between the Dirac wave functions  $\Psi_{n\nu m t_z}$ , and then treat  $\rho(\mathbf{r}', \mathbf{r})$  as nonrelativistic density matrix. The orthogonality of the spin states leads to  $\delta_{m_s, m'_s}$  and thus to  $m_l = m_{l'}$ . Taking advantage of the symmetry properties of the Clebsch-Gordon coefficients leads to

$$\rho(\mathbf{r}', \mathbf{r}) = \sum_{n\nu} \left[ \frac{G_{t_z,n,\nu}(r')}{r'} \frac{G_{t_z,n,\nu}(r)}{r} + \frac{F_{t_z,n,\nu}(r')}{r'} \frac{F_{t_z,n,\nu}(r)}{r} \right] \frac{2j+1}{2l+1} \sum_{m_l} Y_l^{*m_l}(r') Y_l^{m_l}(r). \quad (3.6)$$

The calculation of the full-folding optical potential  $\hat{U}(\mathbf{q}, \mathbf{K})$  requires the nuclear density matrix in momentum space. Thus we need to double Fourier transform  $\rho(\mathbf{r}', \mathbf{r})$  to

obtain the density  $\rho(\tilde{\mathbf{p}}', \tilde{\mathbf{p}})$  in the rest frame of the nucleus. This frame is characterized by the momenta  $\tilde{\mathbf{p}}$  and  $\tilde{\mathbf{p}}'$  and the density matrix is obtained by

$$\rho_\alpha(\tilde{\mathbf{p}}', \tilde{\mathbf{p}}) = \frac{1}{8\pi^3} \int d^3\mathbf{r}' e^{-i\mathbf{r}' \cdot \tilde{\mathbf{p}}'} \int d^3\mathbf{r} e^{i\mathbf{r} \cdot \tilde{\mathbf{p}}} \rho_\alpha(\mathbf{r}', \mathbf{r}), \quad (3.7)$$

where we again indicate with the index  $\alpha$  that we have to obtain the density matrix for protons as well as neutrons. Using the standard expansion of a plane wave, the angular integration in Eq. (3.7) can be easily carried out, and we obtain for the density matrix

$$\begin{aligned} \rho_\alpha(\tilde{\mathbf{p}}', \tilde{\mathbf{p}}) = & \frac{1}{2\pi^2} \sum_J (2J+1) \sum_l P_l(\cos \theta_{\tilde{\mathbf{p}}, \tilde{\mathbf{p}}'}) \\ & [ \int dr' r' j_l(\tilde{p}' r') F_{\alpha, t_z, n, \nu}(r') \int dr r j_l(\tilde{p} r) F_{\alpha, t_z, n, \nu}(r) + \\ & \int dr' r' j_l(\tilde{p}' r') G_{\alpha, t_z, n, \nu}(r') \int dr r j_l(\tilde{p} r) G_{\alpha, t_z, n, \nu}(r) ]. \end{aligned} \quad (3.8)$$

The density matrix  $\rho_\alpha(\tilde{\mathbf{p}}', \tilde{\mathbf{p}})$  given in Eqs. (3.7) or (3.8) is defined in the rest frame of the nucleus. In order to apply  $\rho_\alpha(\tilde{\mathbf{p}}', \tilde{\mathbf{p}})$  in our calculation of the full-folding optical potential for nucleon-nucleus scattering, we have to evaluate the function at the corresponding momenta in the nucleon-nucleus frame. This is facilitated by variable transformations  $\mathbf{p} = \tilde{\mathbf{p}} - \frac{\mathbf{k}}{\mathbf{A}}$  and  $\mathbf{p}' = \tilde{\mathbf{p}}' - \frac{\mathbf{k}'}{\mathbf{A}}$ , which takes into account recoil. As an aside, not including recoil would mean the transformation  $\mathbf{p}' = \tilde{\mathbf{p}}' - \frac{\mathbf{k}}{\mathbf{A}}$ .

For the calculation of the density matrices derived from a non-relativistic Hartree-Fock Bogolyubov (HFB) calculation based on the Gogny-D1S NN interaction we employ essentially the same procedure as described above. The wave functions are created in  $r$  space by a code provided by Berger [17] and are represented in a axially symmetric harmonic oscillator basis. A double Fourier transform is then performed using the oscillator basis and summing over all harmonic oscillator quantum numbers. This choice of basis takes advantage of the fact that the Fourier transform of a harmonic oscillator is again a harmonic oscillator. The density matrix is given by

$$\rho_\alpha(\tilde{\mathbf{p}}', \tilde{\mathbf{p}}) = \sum_{i, i'} \rho^{i, i'} \varphi_{i'}^\dagger(\tilde{\mathbf{p}}') \varphi_i(\tilde{\mathbf{p}}), \quad (3.9)$$

where the indices  $i, i'$  count the harmonic oscillator basis states and  $\rho^{i, i'}$  is the density matrix in the oscillator basis. Again, the index  $\alpha$  distinguishes between protons and neutrons. The basis states are explicitly given by

$$\varphi_i(\tilde{\mathbf{p}}) = \sum_m A_{i, m_i}(\beta, \gamma) e^{-\beta p_z^2} H_i(\beta, \tilde{p}_z) e^{-\gamma p_r^2} L_i^{|m|}(\gamma, \tilde{p}_r) e^{im\theta}. \quad (3.10)$$

Here  $\tilde{p}_z$  is the projection of the momentum along the  $z$ -axis and  $p_r$  the radial momentum,  $\beta, \gamma$  are harmonic oscillator constants.  $H_i(\beta, \tilde{p}_z)$  are the Hermite polynomials and  $L_i^{|m|}(\gamma, \tilde{p}_r)$  the Laguerre polynomials. The size of the harmonic oscillator basis used depends on the size of the nucleus, *e.g.* the size of the basis for  $^{16}\text{O}$  is 12 shells whereas for  $^{90}\text{Zr}$  it is 16 shells. It should be noted that the indices  $i$  and  $i'$  are not independent. The size of the basis sets needed makes the calculation of  $\rho_\alpha(\tilde{\mathbf{p}}', \tilde{\mathbf{p}})$  quite lengthy, especially for heavier nuclei.



In order to calculate the optical potential  $\hat{U}(\mathbf{q}, \mathbf{K})$  as given in Eq. (2.25), we need the density matrix as function of the momentum transfer  $\mathbf{q}$  and  $\mathbf{P} = \hat{\mathbf{p}} + \frac{\mathbf{K}}{A}$  as indicated in Eq. (2.22). In these variables the density matrix is related to the density profile  $\rho_\alpha(q)$  of the nucleus by

$$\rho_\alpha(q) = \int d^3\mathbf{P} \rho_\alpha\left(\mathbf{P} - \frac{A-1}{A}\frac{\mathbf{q}}{2}, \mathbf{P} + \frac{A-1}{A}\frac{\mathbf{q}}{2}\right). \quad (3.11)$$

The normalization is chosen such that  $\rho_\alpha(q=0) = Z$  or  $N$ , the number of protons or neutrons, respectively.

In practice we used the relation given in Eq. (3.11) for testing our numerical integration schemes with the simple harmonic oscillator density given in Ref. [3]. In order to determine how well the two model density matrices presented here describe the experimentally determined proton distribution, we calculate the proton density profiles  $\rho_p(q)$  for both the DH and the HFB models for each nucleus we consider. In the following we want to discuss two cases, namely  $^{16}\text{O}$  and  $^{90}\text{Zr}$ . In Fig. 2 we compare the density profiles calculated from the DH and HFB models to the experimental proton distribution [20]. Overall the DH profile follows the experimental distribution closer than the HFB profile. The HFB profile is shifted to larger momenta indicating that the HFB model slightly underpredicts the radius of the proton distribution of  $^{16}\text{O}$ . This feature will be visible in the proton-scattering observables for  $^{16}\text{O}$  calculated with the HFB model. In the close-up of the minimum of the density profile it can be seen that both model densities slightly deviate from the experimental profile. In Fig. 3 we carry out the same comparison for a heavier nucleus,  $^{90}\text{Zr}$ . Here both model densities follow the experimental proton distribution [20] very closely. The close-up of the minimum reveals that the HFB profile deviates only slightly from the experimental profile. This is a general trend, the heavier nuclei are better described by the model profiles. In fact, the proton distribution of  $^{16}\text{O}$  represents the worst case of disagreement of the model profiles with the experimental profiles. This is understandable since the HFB model is known to provide a better representation of the larger nuclei.

## IV. RESULTS AND DISCUSSION

### A. Details of the Calculation

In this paper the study of the elastic scattering of neutrons and protons from spin-zero target nuclei at energies that range from 65 to 400 MeV (incident projectile energy) is strictly first order in the spectator expansion. Here the connection to the propagator  $G_0(E)$  due to the coupling of the initially struck target nucleon to the residual target is considered to be first-order. The full-folding optical potential is calculated as outlined in Section II, specifically as given in Eq. (2.25), using the model densities described in Section III. The calculations for scattering at energies smaller than 200 MeV take into account the coupling of the struck target nucleon to the residual nucleus via the mean field potential  $W_i$ , which is chosen to be consistent with the model density employed. Details of this procedure are given in Refs. [1,11]. Calculations using the Dirac-Hartree densities (and the corresponding potential  $W_i$ ) are labeled DH, while those using the Hartree-Fock-Bogolyubov densities (and corresponding potentials  $W_i$ ) are labeled HFB.

The convolution of the fully off-shell density matrix  $\rho_\alpha$  with the fully off-shell NN t-matrix, and the Møller frame transformation factor  $\eta(\mathbf{P}, \mathbf{q}, \mathbf{K})$  as given in Eq. (2.24) is carried out in three dimensions without partial wave decomposition and the integration is performed using Monte Carlo integration techniques. Our algorithm uses Quasi-Random numbers [21], together with importance sampling, which according to our tests has the advantage of needing significantly fewer integration points than algorithms based on conventional ‘random number’ generators or Gauss-Legendre integration to obtain the same accuracy. Quasi random numbers provide a ‘uniform’ random distribution over the integration space.

Aside from the density matrices, the fully off-shell NN t-matrix is another crucial ingredient in the calculation of  $\hat{U}(\mathbf{q}, \mathbf{K})$ . The calculations presented use the free NN interaction based upon the full Bonn potential [22]. This interaction includes the effects of relativistic kinematics, retarded meson propagators as given by time-ordered perturbation theory, and iterative and crossed meson-exchanges with  $NN$ ,  $N\Delta$ , and  $\Delta\Delta$  intermediate states. For the calculations involving projectile energies greater than 300 MeV we employ an extension of the Bonn model above pion-production threshold [15]. In this model pion production is described through the decay of the delta isobar with a width obtained consistently from the imaginary part of the one-pion loop diagram for the delta self-energy. It is also to be understood that we perform all spin summations in obtaining  $\hat{U}(\mathbf{q}, \mathbf{K})$ . This reduces the required NN t-matrix elements to a spin independent component (corresponding to the Wolfenstein amplitude A) and a spin-orbit component (corresponding to the Wolfenstein amplitude C). Since we are assuming that we have spin saturated nuclei, the components of the NN t-matrix depending on the spin of the struck nucleon vanish. For the proton nucleus scattering calculations the Coulomb interaction between the projectile and the target is included using the exact formulation described in Ref. [27].

A common approximation to the full-folding expression of Eq. (2.25), which still preserves the non-local character of the NN t-matrix, is obtained as follows. If one observes that the nuclear size is significantly larger than the range of the NN interaction, the amplitude  $\hat{\tau}_\alpha$  is expected to be the slower varying quantity in the integral of Eq. (2.25). This argues for the method of optimum factorization [13,24] which proceeds via an expansion of  $\hat{\tau}_\alpha$  (including the factor  $\eta(\mathbf{q}, \mathbf{K}, \mathbf{P})$ ) in  $\mathbf{P}$  about a fixed value  $\mathbf{P}_0$ . The reference momentum  $\mathbf{P}_0$  is determined by requiring that the contribution of the first derivative term be minimized. In the elastic scattering case this contribution can be made to vanish if  $\mathbf{P}_0$  is chosen to be zero. For further details we refer to Ref [13]. After the integration over the density matrix to produce the diagonal density profile  $\rho_\alpha(q)$  (Eq. (3.11)) the ‘optimum factorized’ or ‘off-shell  $t\rho$ ’ form of the optical potential is given by

$$\hat{U}_{fac}(\mathbf{q}, \mathbf{K}) = \sum_{\alpha=p,n} \eta(\mathbf{q}, \mathbf{K}) \hat{\tau}_\alpha \left( \mathbf{q}, \frac{A+1}{2A} \mathbf{K}, \epsilon \right) \rho_\alpha(q) \quad (4.1)$$

Here the non-local character of the optical potential is solely determined by the off-shell NN t-matrix. For harmonic oscillator model densities it has been shown for light nuclei that the optimum factorized form represents the non-local character of  $\hat{U}(\mathbf{q}, \mathbf{K})$  qualitatively [2,3] when applied within the KMT formalism to first order at intermediate energies. When comparing elastic scattering observables obtained from full-folding optical potentials to those obtained from ‘off-shell  $t\rho$ ’ optical potentials, the scope is two-fold. First, we employ here realistic models of the nuclear density for light as well as heavy nuclei. Second we extend this

comparison toward energies below 100 MeV where it could be expected that the nucleon-nucleus scattering calculation samples the optical potential further off-shell and thus the optimum factorized form may not be as good an approximation.

## B. Elastic Scattering Results

Elastic scattering calculations from several spherical nuclei are carried out at a variety of energies between 65 and 400 MeV to allow for comparisons between results obtained from the full-folding optical potentials with those arising from the factorized off-shell ‘ $t\rho$ ’ approximation.

The scattering observables for elastic proton scattering from  $^{16}\text{O}$  are displayed in Fig. 4. The solid line represents the calculation with the full-folding optical potential based on the DH density and the Bonn t-matrix defined above pion-production threshold, while the dashed line represents the optimum factorized form as defined in Eq. (4.1). Both calculations are based on the free NN t-matrix. Since the two calculations give very similar results, it can be concluded that the bulk of the non-locality of the optical potential, which affects the elastic scattering observables, must come from the off-shell structure of the NN t-matrix. The off-shell structure of the nuclear density matrix plays an insignificant role for elastic scattering observables at these high energies. A similar conclusion was already drawn in Ref. [3] and is here confirmed using realistic densities. In order to illustrate the effect of the different density profiles for the DH and the HFB models (as shown in Fig. 2) on the elastic observables, we display two calculations based on the factorized optical potential for the DH (solid line) and the HFB model (dashed line) in Fig. 5. As already discussed in Section III, especially in the case of  $^{16}\text{O}$ , the HFB density profile is shifted to larger momenta compared to the DH profile. This translates directly into a slight shift of the first minimum of the differential cross-section to larger angles and a slightly smaller angular spacing of the diffraction minima. We carried out similar comparisons of full-folding and optimum factorized optical potentials for heavier nuclei, but there the disagreement between the density profiles of the two models is much smaller than for  $^{16}\text{O}$  and consequently the prediction of the observables are very similar.

Another effect worthwhile to study in this context is the influence of the Møller factor [14], which takes into account the transformation of the NN t-matrix evaluated in the NN c.m. frame to the zero momentum frame of the nucleon-nucleus system. This frame transformation can be viewed as a relativistic effect and its importance should increase with higher scattering energies. For these reasons we want to consider its effect on the elastic scattering observables for proton scattering from  $^{16}\text{O}$  at 500 MeV (Fig. 6). The Møller factor  $\eta(\mathbf{P}, \mathbf{q}, \mathbf{K})$  as given in Eq. (2.24) is a function of three vector momenta and is part of the full-folding integral of Eq. (2.25). The solid line in Fig. 6 represents the calculation of  $\hat{U}(\mathbf{q}, \mathbf{K})$  as given in Eq. (2.25). In the spirit of the optimum factorized approximation  $\eta(\mathbf{P}, \mathbf{q}, \mathbf{K})$  can be expanded around a fixed value  $\mathbf{P}_0$  (here  $\mathbf{P}_0=0$ ), thus becoming independent of the integration variable  $\mathbf{P}$ . This expansion corresponds to considering  $\eta(\mathbf{q}, \mathbf{K})$  at a fixed angle between  $\mathbf{q}$  and  $\mathbf{K}$ , specifically here  $\Theta = 90^\circ$ . The dashed line therefore in Fig. 6 corresponds to evaluating the optical potential according to

$$\hat{U}(\mathbf{q}, \mathbf{K}) = \sum_{\alpha=p,n} \eta(\mathbf{q}, \mathbf{K})_{\Theta=90^\circ} \int d^3\mathbf{P} \hat{\tau}_\alpha \left( \mathbf{q}, \frac{1}{2} \left( \frac{A+1}{A} \mathbf{K} - \mathbf{P} \right); \epsilon \right) \rho_\alpha \left( \mathbf{P} - \frac{A-1}{A} \frac{\mathbf{q}}{2}, \mathbf{P} + \frac{A-1}{A} \frac{\mathbf{q}}{2} \right) \quad (4.2)$$

The dashed and solid lines in Fig. 6 are almost indistinguishable. This infers the conclusion that  $\eta(\mathbf{q}, \mathbf{K})_{\Theta=90^\circ}$  is a very good representation of the exact expression given in Eq. (2.24). In order to illustrate the total effect due to the inclusion of the Møller factor, the dotted line in Fig. 6 represents a calculation with  $\eta(\mathbf{q}, \mathbf{K})$  set to one in Eq. (4.2).

At energies below 200 MeV, calculations of elastic observables not only incorporate the effects of the nuclear structure models within the full-folding procedure but also via the mean field force (given by the structure model) which couples the struck target nucleon to the residual nucleus. Thus it is hoped that the influence of different structure models on the elastic observables is observable. In Fig. 7 we display the elastic observables for proton scattering from  $^{40}\text{Ca}$  at 100 MeV laboratory energy employing the DH model for the density as well as the mean field force  $W_i$ . In Fig. 8 the corresponding calculation is done using the HFB model. In both figures the solid line represents the full-folding calculation, and the dashed line the factorized off-shell ‘ $t\rho$ ’ approximation. All calculations contain the modification due to the mean field  $W_i$ . The off-shell structure of the nuclear density matrix in the full-folding procedure has at this lower energy a slightly larger effect on the spin observables than at higher energies. In addition, the angular distribution of the differential cross section diffracts at slightly larger angles in the full-folding calculations compared to those based on the factorized form. This trend is also observed for the heavier nuclei  $^{90}\text{Zr}$  and  $^{208}\text{Pb}$  (Figs. 9 and 10).

The elastic observables for proton scattering from  $^{90}\text{Zr}$  at 80 MeV are displayed in Fig. 9. Here the difference between the two model densities employed is almost negligible for  $\frac{d\sigma}{d\Omega}$  and  $A_y$ . Only for the spin rotation function the difference given by using two different structure models is at higher angles as large as the effect of using the factorized approximation. This result, namely that the observables predicted by the two different models under consideration are so similar, is not surprising in that both models predict an almost identical density profile (Fig. 3). The effect of the off-shell structure of the nuclear density matrix is relatively small as the comparison between the full-folding (solid) line and corresponding factorized (dashed) calculation shows. In the case of proton scattering from  $^{208}\text{Pb}$  at 65 MeV (Fig. 10) a comparison between a full-folding calculation and the factorized approximation reveals the same trends as the observables for the lighter nuclei. At large angles the full-folding calculation falls below the one given by the factorized form, and in this case also below the data. The inclusion of the off-shell structure of the nuclear density matrix makes the nucleus appear slightly larger, which becomes apparent in the shifted diffraction pattern of  $\frac{d\sigma}{d\Omega}$ .

It is difficult to extract properties of nonlocal potentials from elastic scattering observables. Nonlocal effects are presumably more important in inelastic processes which depend on the nucleon-nucleus interaction such as quasielastic electron scattering reactions. In order to gain more insight into the difference between a full-folding optical potential and the factorized off-shell ‘ $t\rho$ ’ approximation to this potential, we plot in Figs. 11 ( $^{40}\text{Ca}$ ) and 14 ( $^{208}\text{Pb}$ ) the real and imaginary parts of the on-shell value of  $\hat{U}(\mathbf{q}, \mathbf{K})$  as a function of the orbital angular momentum  $L$ . We separate the cases  $J = L + \frac{1}{2}$  and  $J = L - \frac{1}{2}$  to isolate the

effect of the spin-orbit force. As is seen in both figures, the full-folding (solid lines) and the factorized (dashed lines) on-shell values of the imaginary parts of the optical potential are quite similar. In both cases the real part of the on-shell values of the optical potentials exhibit an increasing suppression for smaller  $L$  as the nonlocal effects of the density matrix as well as the NN  $t$ -matrix are treated more adequately in the full-folding procedure. It should be emphasized again that Figs. 11 and 14 only show the value of  $\hat{U}(\mathbf{q}, \mathbf{K})$  fulfilling the on-shell condition  $\mathbf{q} \cdot \mathbf{K} = 0$  and  $\mathbf{q}^2 + 4\mathbf{K}^2 = 4\mathbf{k}_0^2$  with  $\mathbf{k}_0$  being the on-shell relative momentum for proton-nucleus (NA) scattering and do not display any off-shell behavior inherent in the potentials. After iteration to obtain the Watson optical potential (Eq. 2.11) and then in the integral equation (Eq. 2.9), the on-shell elements of the NA  $t$ -matrix display much smaller differences between the full-folding and its factorized, on-shell ' $t\rho$ ' approximation. For  $^{208}\text{Pb}$  the differences in the real parts are nearly insignificant (Fig. 15), whereas for  $^{40}\text{Ca}$  a slight suppression of the real part for small  $L$  remains for the full-folding calculation compared to the factorized approximation. However, the differences occur mainly for smaller  $L$  where the imaginary part of the potentials as well as the  $t$ -matrices are relatively large. Because the absorption is significant for these low partial waves, the elastic observables are not particularly sensitive to the differences in the real parts as displayed in Figs. 13 and 16.

In Fig. 17 total neutron cross section data for  $^{12}\text{C}$ ,  $^{16}\text{O}$ ,  $^{28}\text{Si}$ ,  $^{40}\text{Ca}$ ,  $^{90}\text{Zr}$ , and  $^{208}\text{Pb}$  are shown along with various calculations of  $\sigma_{tot}(E)$  at a number of energies. Because the data are so extensive, the 'usual' procedure has been reversed in the plotting of these cross sections so that the data are represented by dotted curves, and the discrete points correspond to calculated results. The solid diamonds represent the full-folding calculations as described in Section II. All calculations are based on a DH model for the nuclear density. For energies  $\leq 200$  MeV the modification of the free propagator through the DH mean field is included as described in Ref. [11]. It has been shown in Ref. [1] that for higher energies this modification of the free propagator becomes negligible. The open circles represent calculations based on the factorized, off-shell ' $t\rho$ ' form using the same NN  $t$ -matrix. A general trend to be observed in Fig. 17 is the slightly lower value of  $\sigma_{tot}(E)$  obtained from a full-folding calculation compared to the factorized approximation. This trend is almost independent of the energy and the nucleus under consideration and is consistent with the observation that full-folding calculations of the differential cross sections fell slightly below the values given by a factorized calculation.

At this point it is worthwhile to investigate whether the interactions of the projectile with the target nucleus is uniformly distributed over the entire nucleus or if specific regions of the nucleus play a more dominant role in the scattering process at intermediate energies. For our study we chose neutron scattering at 200 MeV projectile energy and consider contributions from specific shells to the total cross sections. We employ the DH model for the density and remove outer shells of protons as well as neutrons. Then we recalculate the scattering from the remaining 'inner core', which is chosen to be doubly magic, so that it is bound. The results of this procedure for  $^{16}\text{O}$ ,  $^{40}\text{Ca}$ , and  $^{208}\text{Pb}$  are given in Table I. As a technical detail, when calculating the scattering in these tests we treated the targets as being infinitely heavy to exclude recoil effects, which would be larger for smaller cores. In order to give an estimate of the size of the recoil effect on the total cross section we give the values of  $\sigma_{tot}$  calculated with and without recoil in Table I. The values for the total cross section for neutron scattering for 'inner cores' of 100, 40, 16, and 4 nucleons are given as

entries of the corresponding nuclei. The entries in Table I marked ‘n.b.’ indicate that e.g. in the case of  $^{208}\text{Pb}$  the DH calculation with only 8 neutrons and 8 protons did not result in a bound system using the parameters of  $^{208}\text{Pb}$  given for those 16 nuclei. The calculated rms radii for the ‘inner cores’ under consideration for  $^{16}\text{O}$ ,  $^{40}\text{Ca}$ , and  $^{208}\text{Pb}$  are listed in Table II. This table also contains the rms radii for the proton and neutron distributions for the above mentioned nuclei as given by the DH model. Columns 3 and 4 of Table II compare the percentage of the volume filled by the ‘inner core’ if either the corresponding rms radius is used (column 3) or the radius is taken to be proportional to  $A^{\frac{1}{3}}$  (column 4). The percentage Of the calculated total cross section contribution from the inner core nucleus is given in column 5. The numbers suggest that the nucleons in the interior of the nucleus contribute to the total cross sections with a percentage slightly larger then the volume they occupy when the volume is based on the crude estimate  $r \sim A^{\frac{1}{3}}$ . This leads to the conclusion that all nucleons in the nucleus almost equally contribute to the scattering process. We performed a similar study at 100 MeV and 500 MeV projectile energy and did not find any significant deviations from the ratios  $\sigma_{tot}(\text{core})/\sigma_{tot}$  as given in Table II at 200 MeV.

## V. CONCLUSION

We have calculated the full-folding integral for the first-order optical potential within the framework of the spectator expansion of multiple scattering theory. These optical potentials are based on realistic models for the nuclear density matrix, namely a Dirac-Hartree and a Hartree-Fock-Bogolyubov model along with the full Bonn meson exchange model for the NN t-matrix. Recoil and frame transformation factors are implemented in the calculation in their complete form. We calculated elastic scattering observables for a variety of light and heavy nuclei at projectile energies from 65 to  $\sim 400$  MeV laboratory energy. At energies below 200 MeV we included the modification of the free propagator due to the coupling of the struck target nucleon to the residual nucleus via the same mean field used to model the effect of the nuclear medium is intrinsically consistent with the nuclear structure. The predictions from these rigorous calculations of elastic nucleon nucleus observables provide excellent agreement with the experimental data in this energy regime.

We tested the validity of the factorized off-shell ‘ $t\rho$ ’ approximation in the energy regime between 65 and 400 MeV and found that this approximation, which only retains the non-locality given through the NN t-matrix, is even at lower energies a very good representation of the full-folding calculation as far as the elastic nucleon-nucleus observables are concerned. Differences between the factorized approximation and the full calculation of the optical potential are present predominantly in lower partial waves. However due to the cumulative effect of many partial waves the elastic observables do not reflect these differences. It should be noted that in *e.g.* inelastic scattering of nucleons from nuclei or quasielastic electron scattering those differences between full-folding calculations and the corresponding factorized approximation may become more significant. We also studied the contribution of the interior structure of the nucleus to the total cross section and find that all nucleons in the nucleus contribute almost uniformly to the scattering process.

## ACKNOWLEDGMENTS

The authors want to express their gratitude and appreciation towards R.M. Thaler for the many stimulating, helpful and critical discussions during the major stages of this project.

This work was performed in part under the auspices of the U. S. Department of Energy under contracts No. DE-FG02-93ER40756 with Ohio University, DE-AC05-84OR21400 with Martin Marietta Energy Systems, Inc., and DE-FG05-87ER40376 with Vanderbilt University. We thank the Arctic Region Supercomputing Center (ARSC) and the Ohio Supercomputer Center (OSC) for the use of their facilities. These resources were made available through the metacenter regional alliance project funded by the Advanced Scientific Computing Program of the National Science Foundation, Award number ASC-9418357 and Grant No. PHS206 from OSC. We also thank the Pittsburgh Supercomputer Center (PSC) for the use of their facilities under Grant No. PHY950010P as well as the National Energy Research Supercomputer Center (NERSC) for the use of their facilities under the FY1996 Massively Parallel Processing Access Program.

## REFERENCES

- [1] C.R. Chinn, Ch. Elster, R.M. Thaler, and S.P. Weppner, Phys. Rev. **C52**, 1992 (1995).
- [2] R. Crespo, R.C. Johnson, and J.A. Tostevin, Phys. Rev. **C41**, 2257 (1990).
- [3] T. Cheon, Ch. Elster, E.F. Redish, and P.C. Tandy, Phys. Rev. **C41**, 841 (1990).
- [4] H.F. Arellano, F.A. Brieva, M. Sander, H.V. von Geramb, Phys. Rev. **C54**, 2570 (1996).
- [5] H.F. Arellano, F.A. Brieva, and W.G. Love, Phys. Rev. **C52**, 301 (1995); H.F. Arellano, F.A. Brieva, and W.G. Love, Phys. Rev. **C41**, 2188 (1990).
- [6] D.J. Ernst, J.T. Londergan, G.A. Miller, and R.M. Thaler, Phys. Rev. **C16**, 537 (1977).
- [7] E.R. Siciliano and R.M. Thaler, Phys. Rev. **C16**, 1322 (1977).
- [8] P.C. Tandy and R.M. Thaler, Phys. Rev. **C22**, 2321 (1980).
- [9] K.M. Watson, Phys. Rev. **89**, 575 (1953); N.C. Francis and K. M. Watson, *ibid.* **92**, 291 (1953).
- [10] A. Kerman, M. McManus, and R.M. Thaler, Ann. Phys. **8**, 551 (1959).
- [11] C.R. Chinn, Ch. Elster, R.M. Thaler, Phys. Rev. **C48**, 2956 (1993).
- [12] P.C. Tandy, E.F. Redish, and D. Bollé, Phys. Rev. **C16**, 1924 (1977).
- [13] A. Picklesimer, P.C. Tandy, R.M. Thaler, and D. H. Wolfe, Phys. Rev. **C 30**, 1861 (1984).
- [14] C.J. Joachain, ‘Quantum Collision Theory’ (North-Holland Physics 1987) p. 387; C. Møller, Kgl. Danske Videnskab. Selskab., Mat.-fys. Medd **23**, 1 (1959).
- [15] Ch. Elster and P.C. Tandy, Phys. Rev. **C40** (1989), 881.
- [16] C.J. Horowitz and B.D. Serot, Nucl. Phys **A368**, 503 (1981).
- [17] See for example J.F. Berger, M. Girod, and D. Gogny, Nucl. Phys. **A502**, 85c (1989); J.P. Delaroche, M. Girod, J. Libert and I. Deloncle, Phys. Lett. **B232**, 145 (1989).
- [18] J. Dechargé and D. Gogny, Phys. Rev. **C21**, 1568 (1980); J.F. Berger, M. Girod, and D. Gogny, Comput. Phys. Commun. **63**, 365 (1991).
- [19] C.J. Horowitz, D.P. Murdoch, and B.D. Serot, *Computational Nuclear Physics 1*, edited by K. Langanke, J.A. Maruhn, and S.E. Koonin (Springer-Verlag, Berlin, 1991), p. 129 (*includes source code*)
- [20] H. De Vries, C.W. De Jager, and C. De Vries, Atomic and Nuclear Data Tables **36**, 495(1987)
- [21] W.H. Press and S.A. Tenkolsky, Comp. in Phys. **76**(1989)
- [22] R. Machleidt, K. Holinde, and Ch. Elster, Phys. Rep. **149**, (1987).
- [23] C.R. Chinn, Ch. Elster, and R.M. Thaler, Phys. Rev. **C44**, 1569 (1991).
- [24] D.J. Ernst and G.A. Miller, Phys. Rev. **C21**, 1472 (1980); D.L. Weiss and D.J. Ernst, Phys. Rev. **C26**, 605 (1982); D.J. Ernst, G.A. Miller, and D.L. Weiss, Phys. Rev. **C27**, 2733 (1983)
- [25] I. Sick, J. B. Bellicard, J. M. Cavedon, B. Frois, M. Huet, P. Leconte, P. X. Ho, and S. Platchkov, Phys. Lett. **88B**, 245 (1979); B. Frois, J.B. Bellicard, J.M. Cavedon, M. Huet, P. Leconte, P. Ludeau, A. Nakada, and P.X. Ho, Phys. Rev. Lett. **38**, 152 (1977).
- [26] C.R. Chinn, Ch. Elster, and R.M. Thaler, Phys. Rev. **C47**, 2242 (1993).
- [27] C.R. Chinn, Ch. Elster, and R.M. Thaler, Phys. Rev. **C44**, 1569 (1991).
- [28] R. W. Finlay, W. P. Abfalterer, G. Fink, E. Montei, T Adami, P. W. Lisowski, G. L. Morgan and R. C. Haight, Phys. Rev. **C 47**, 237 (1993).
- [29] R.W. Finlay, G. Fink, W. Abfalterer, P. Lisowski, G.L. Morgan, and R.C. Haight, in



- Proceedings of the Internat. Conference on Nuclear Data for Science and Technology*, edited by S.M. Qaim (Springer-Verlag, Berlin, 1992), p. 702.
- [30] C. Chan, M.S. thesis, University of Alberta, 1985; D. Hutcheon, private communication.
  - [31] H. Seifert, Ph.D thesis, Univ. Maryland (1990).
  - [32] P. Schwandt, H.O. Mayer, W.W. Jacobs, A.D. Baches, S.E. Vigdor, M.D. Kartchuck, *Phys. Rev.* **C26**, 55 (1982).
  - [33] H. Sakaguchi, M. Nakamura, K. Hatanaka, A. Goto, T. Noro, F. Ohtani, H. Sakamoto, H. Ogawa, and S. Kobayashi, *Phys. Rev.* **C 26**, 944 (1982).
  - [34] E.J. Stephenson, in ‘Antinucleon- & Nucleon-Nucleus Interactions’ Telluride, Co. 1985, pp 299, ed. by G. Walker et al. (Plenum Press, NY, 1985).
  - [35] D.A. Hutcheon et al. in ‘Polarization Phenomena in Nuclear Physics - 1980’, *Proceedings of the Fifth International Symposium on Polarization Phenomena in Nuclear Physics*, AIP Conf. Proc. No. 69, edited by G.G. Ohlson, R.E. Brown, N. Jarmie, W.W. McNaughton, and G.M. Hale (AIP, NY, 1981), p. 454. The data for  $Q$  are from Na Gi, Masters Thesis, Simon Frazer University, British Columbia, 1987.

# TABLES

TABLE I. Total cross sections for neutron scattering from  $^{16}\text{O}$ ,  $^{40}\text{Ca}$ , and  $^{208}\text{Pb}$  as well as from inner shells of those nuclei. The entries printed in boldface are the ones for which the rms-radii and ratios are calculated in Table II.

	$\sigma_{tot}[b]$	$\sigma_{tot}[b]$ no recoil	$\sigma_{tot}[b]$ core of 4	$\sigma_{tot}[b]$ core of 16	$\sigma_{tot}[b]$ core of 40	$\sigma_{tot}[b]$ core of 100
$^{16}\text{O}$	.423	.419	<b>.120</b>	.419		
$^{40}\text{Ca}$	.925	.921	n.b.	<b>.419</b>	.921	
$^{208}\text{Pb}$	3.38	3.37	n.b.	n.b.	<b>.960</b>	2.01

TABLE II. Rms-radii for the proton and neutron distributions of  $^{16}\text{O}$ ,  $^{40}\text{Ca}$ , and  $^{208}\text{Pb}$  as well as from inner shells (cores). The last three columns give the ratios of the volumes of the cores to the total nucleus as well as the ratios of the calculated total neutron cross sections. The numbers used to determine the latter are the ones printed in bold in Table I.

	rms-radius(full)[fm] (proton,neutron)	rms-radius(core)[fm] [core]:(proton,neutron)	$\frac{\langle rms_{core}^3 \rangle}{\langle rms^3 \rangle}$	$\frac{A_{core}}{A}$	$\frac{\sigma_{tot}(core)}{\sigma_{tot}}$
$^{16}\text{O}$	(2.63, 2.60)	[4]:(1.96, 1.95)	42%	25%	29%
$^{40}\text{Ca}$	(3.39, 3.33)	[16]:(2.63, 2.60)	48%	40%	45%
$^{208}\text{Pb}$	(5.40, 5.67)	[40]:(3.72, 4.91)	47%	19%	29%

## FIGURES

FIG. 1. Diagram for the optical potential matrix element for the single-scattering term.

FIG. 2. Comparison of the experimental proton density profile  $\rho_p(q)$  for  $^{16}\text{O}$  [20] (solid line) with the calculated proton density profiles from the DH model (dash-dotted line) and the HFB model (dashed line).

FIG. 3. Comparison of the experimental proton density profile  $\rho_p(q)$  for  $^{90}\text{Zr}$  [20] (solid line) with the calculated proton density profiles from the DH model (dash-dotted line) and the HFB model (dashed line).

FIG. 4. The angular distribution of the differential cross-section ( $\frac{d\sigma}{d\Omega}$ ), analyzing power ( $A_y$ ) and spin rotation function ( $Q$ ) are shown for elastic proton scattering from  $^{16}\text{O}$  at 400 MeV laboratory energy. The solid line represents the calculation performed with a first-order full-folding optical potential based on the DH density [16] and the Bonn model D52 [15]. The dashed line represent the calculation using the factorized, off-shell ‘ $t\rho$ ’ approximation to this optical potential. The data are taken from Ref. [30].

FIG. 5. Same as Fig. 4, except that all calculations are based on the factorized, off-shell ‘ $t\rho$ ’ approximation. The solid line represents the calculation using the DH [16] density profile, whereas the dashed line uses the HFB [17] density profile.

FIG. 6. The angular distribution of the differential cross-section ( $\frac{d\sigma}{d\Omega}$ ), analyzing power ( $A_y$ ) and spin rotation function ( $Q$ ) are shown for elastic proton scattering from  $^{16}\text{O}$  at 500 MeV laboratory energy. The solid line represent the calculation performed with a first-order full-folding optical potential as described in Section II. The dashed line represents a calculation where the Møller factor is evaluated for the fixed angle  $\Theta = 90^\circ$ , whereas for the dotted line the Møller factor was omitted altogether. All calculations are based on the DH density and the Bonn model D52 t-matrix.

FIG. 7. The angular distribution of the differential cross-section ( $\frac{d\sigma}{d\Omega}$ ), analyzing power ( $A_y$ ) and spin rotation function ( $Q$ ) are shown for elastic proton scattering from  $^{40}\text{Ca}$  at 100 MeV laboratory energy. The solid line represent the calculation performed with a first-order full-folding optical potential based on the DH density [16] and the full Bonn model [22], the dashed curve is based on the factorized, off-shell ‘ $t\rho$ ’ approximations. The data are taken from Ref. [31].

FIG. 8. Same as Fig. 7, except that the HFB model [17] is employed for the density as well as the mean field force.

FIG. 9. The angular distribution of the differential cross-section ( $\frac{d\sigma}{d\Omega}$ ), analyzing power ( $A_y$ ) and spin rotation function ( $Q$ ) are shown for elastic proton scattering from  $^{90}\text{Zr}$  at 80 MeV laboratory energy. The solid line represent the calculation performed with a first-order full-folding optical potential based on the DH density [16] and the full Bonn model [22], the dashed curve is based on the factorized, off-shell ' $t\rho$ ' approximations. The dotted line represents a full-folding calculations based on the HFB model [17]. The data are taken from Ref. [32].

FIG. 10. The angular distribution of the differential cross-section ( $\frac{d\sigma}{d\Omega}$ ), analyzing power ( $A_y$ ) and spin rotation function ( $Q$ ) are shown for elastic proton scattering from  $^{208}\text{Pb}$  at 65 MeV laboratory energy. The solid line represent the calculation performed with a first-order full-folding optical potential based on the DH density [16] and the full Bonn model [22], the dashed curve is based on the factorized, off-shell ' $t\rho$ ' approximations. The data are taken from Ref. [33].

FIG. 11. Real and imaginary part of the on-shell value of the optical potential as function of the orbital angular momentum  $L$  for scattering from  $^{40}\text{Ca}$  at 200 MeV laboratory energy. (+) denotes the potential for  $J = L + \frac{1}{2}$ , whereas (-) stand for  $J = L - \frac{1}{2}$ . The full-folding (solid) and factorized, off-shell (dashed) calculations are based on the full Bonn model and the DH density.

FIG. 12. Real and imaginary part of the on-shell value of the proton-nucleus t-matrix (coulomb contributions omitted) as function of the orbital angular momentum  $L$  for scattering from  $^{40}\text{Ca}$  at 200 MeV laboratory energy. (+) denotes the potential for  $J = L + \frac{1}{2}$ , whereas (-) stand for  $J = L - \frac{1}{2}$ . The full-folding (solid) and factorized, off-shell (dashed) calculations are based on the full Bonn model and the DH density.

FIG. 13. The angular distribution of the differential cross-section ( $\frac{d\sigma}{d\Omega}$ ), analyzing power ( $A_y$ ) and spin rotation function ( $Q$ ) are shown for elastic proton scattering from  $^{40}\text{Ca}$  at 200 MeV laboratory energy. The solid line represent the calculation performed with a first-order full-folding optical potential based on the DH density [16] and the full Bonn model [22], the dashed curve is based on the factorized, off-shell ' $t\rho$ ' approximation. The data are taken from Ref. [34].

FIG. 14. Same as Fig. 11, except for  $^{208}\text{Pb}$ .

FIG. 15. Same as Fig. 12, except for  $^{208}\text{Pb}$ .

FIG. 16. Same as Fig. 13, except for  $^{208}\text{Pb}$ . The data are taken from Ref. [35].

FIG. 17. The neutron-nucleus total cross-sections for scattering from  $^{12}\text{C}$ ,  $^{16}\text{O}$ ,  $^{28}\text{Si}$ ,  $^{40}\text{Ca}$ ,  $^{90}\text{Zr}$ , and  $^{208}\text{Pb}$  are shown as a function of the incident neutron kinetic energy. The dotted line represents the data taken from Ref. [28,29]. The solid diamonds correspond to the full-folding calculations using the full Bonn NN t-matrix [22] and the DH model [16] for the density. The open circles correspond to the factorized, off-shell ' $t\rho$ ' approximation. The calculations for energies smaller and equal 200 MeV include the propagator modification due to the DH mean field.

**Fig. 1**

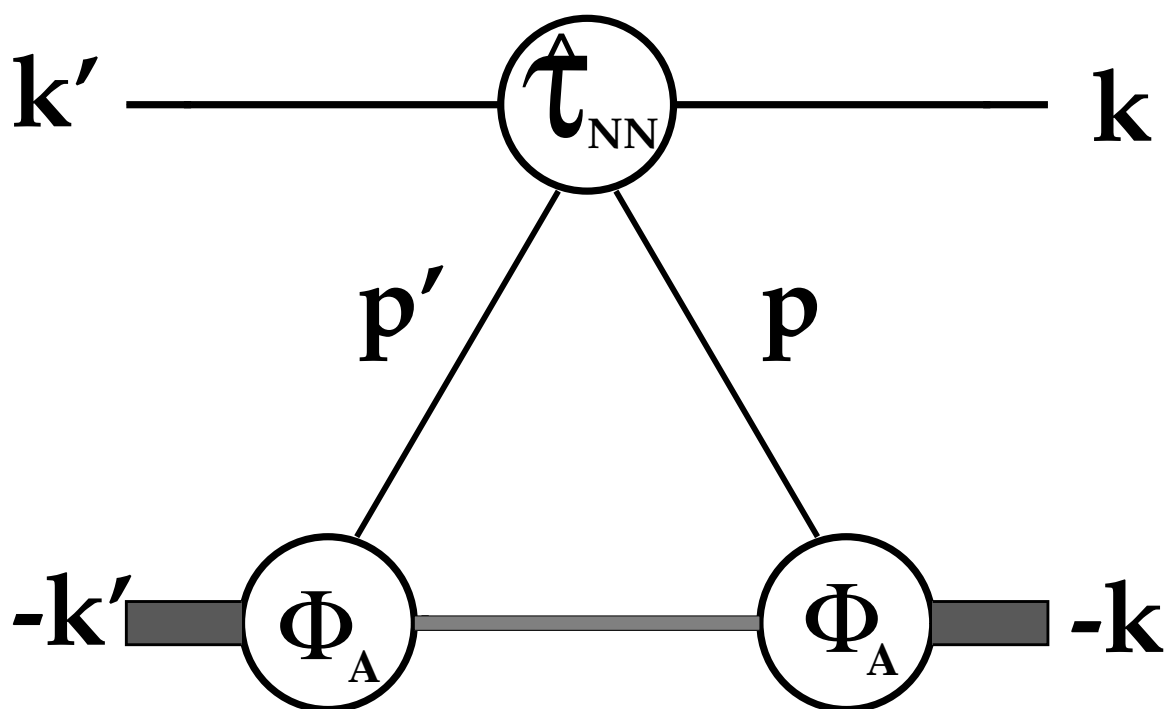


Fig. 2

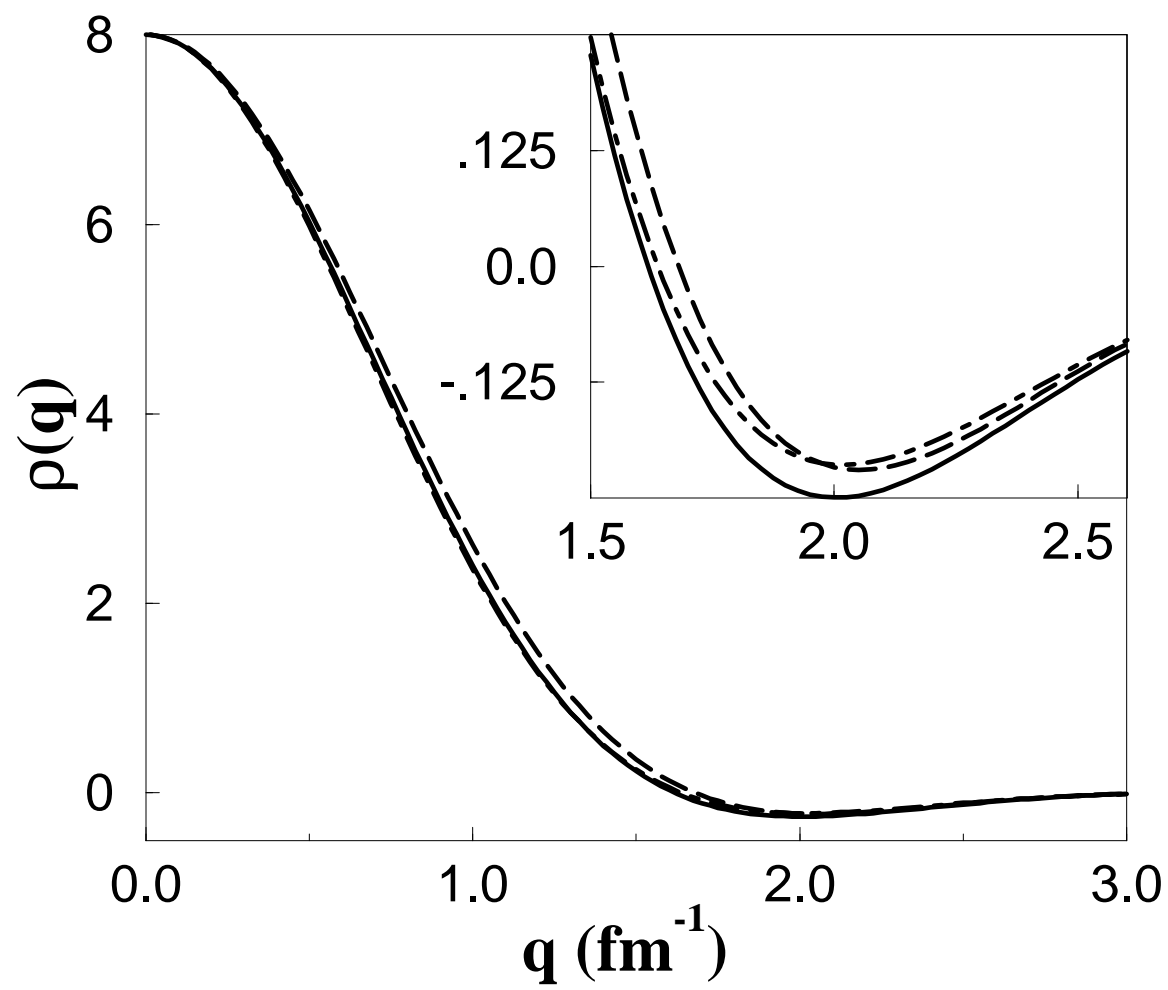


Fig. 3

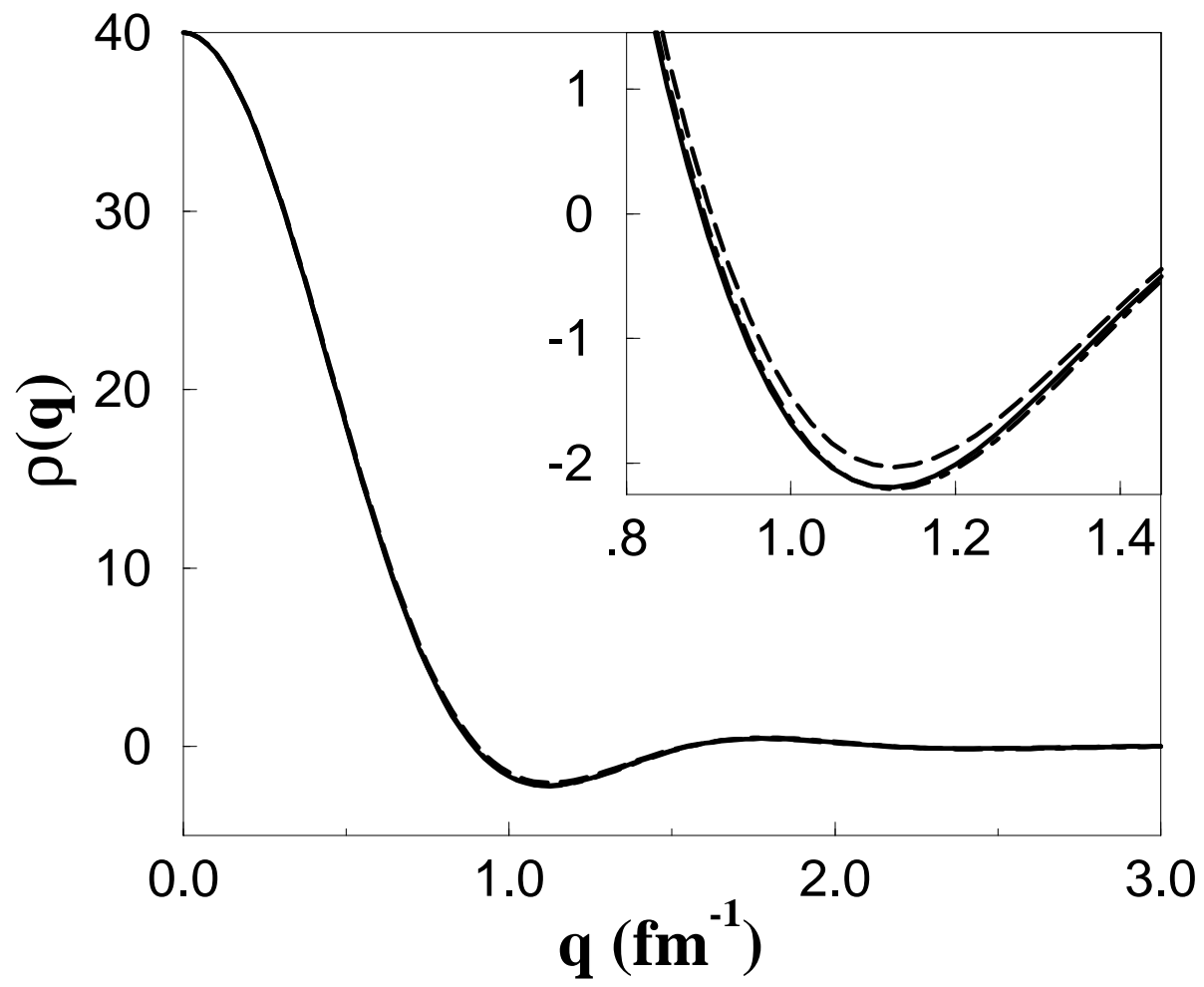




Fig. 4

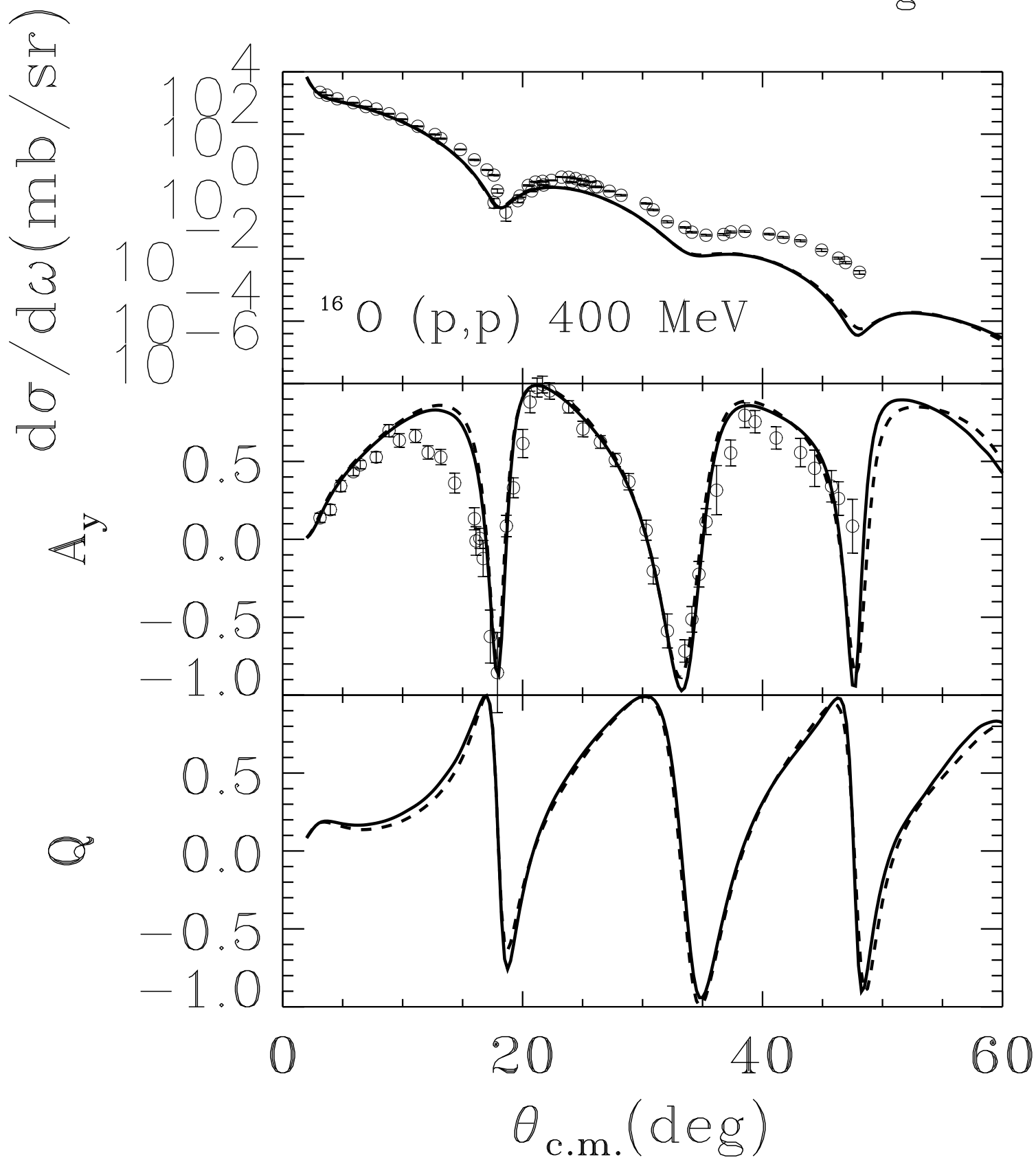


Fig. 5

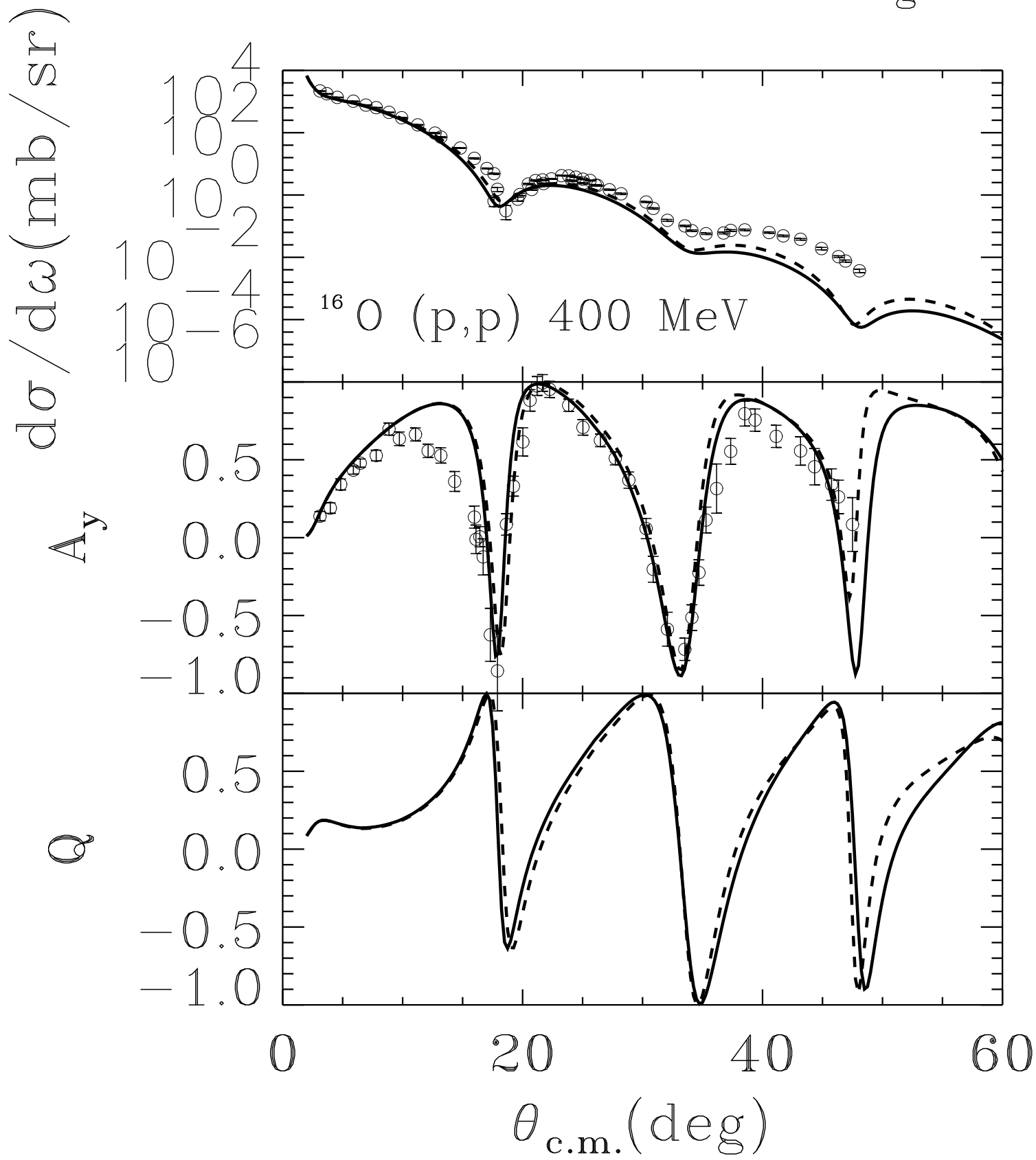


Fig. 6

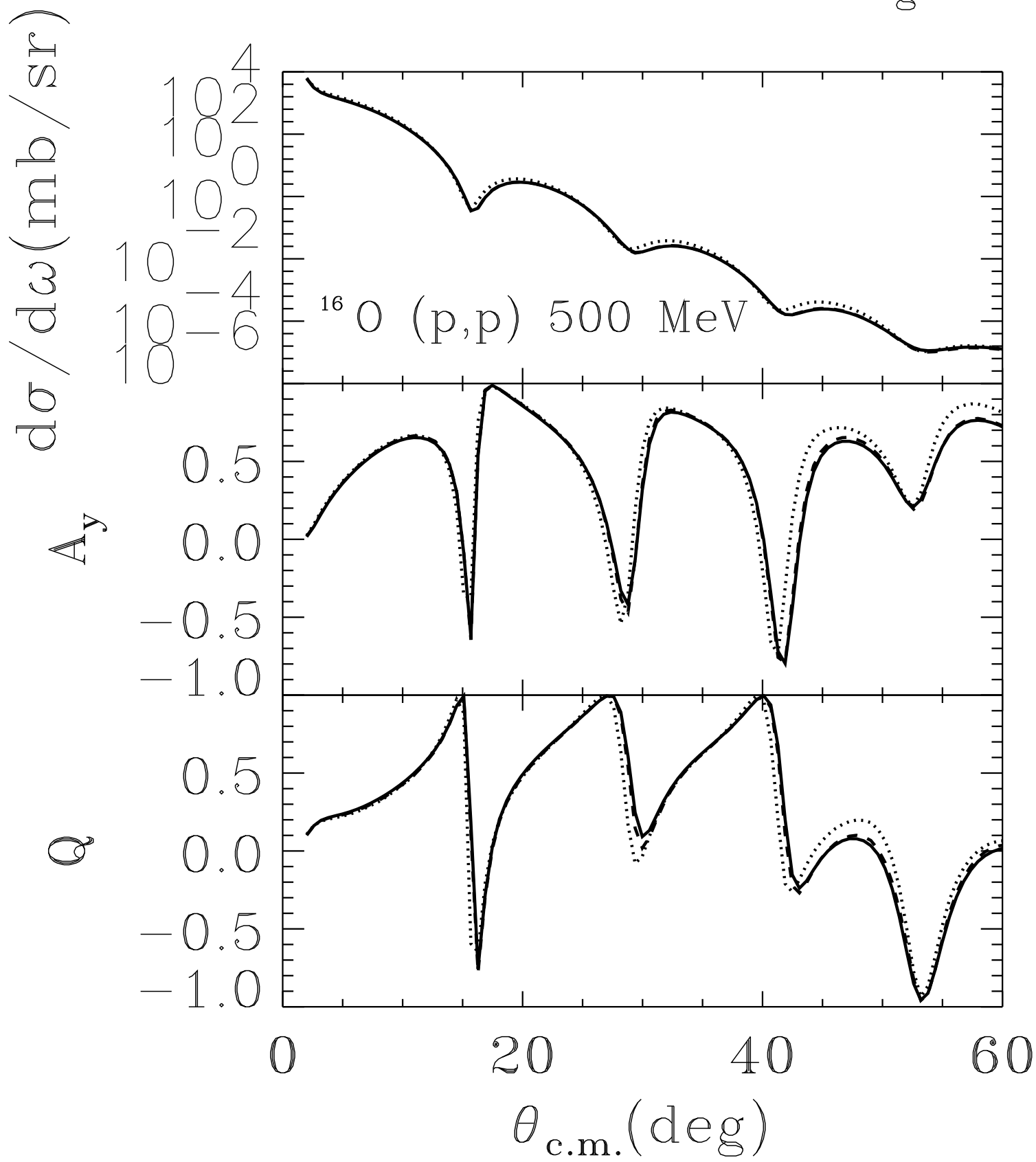


Fig. 7

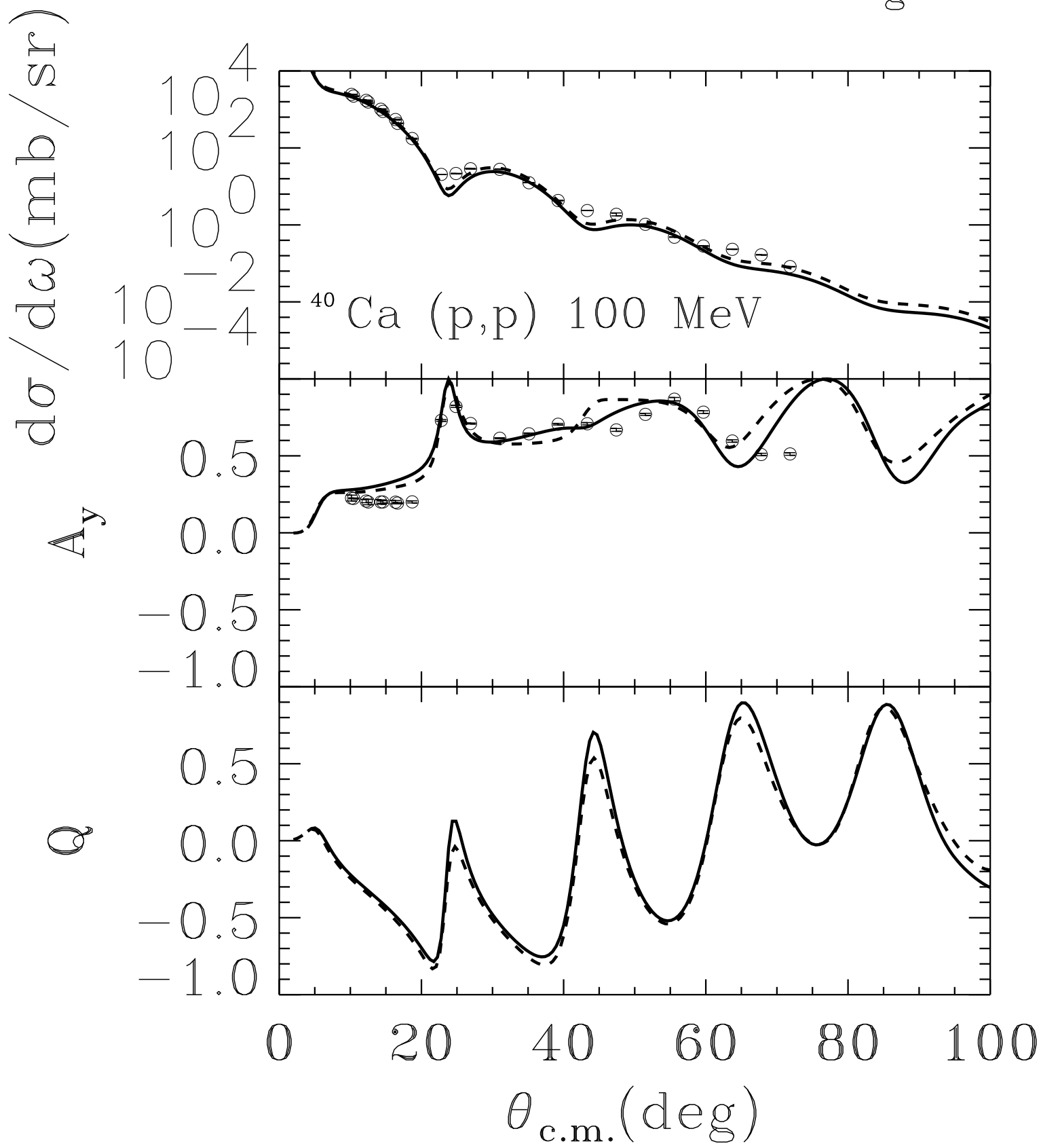


Fig. 8

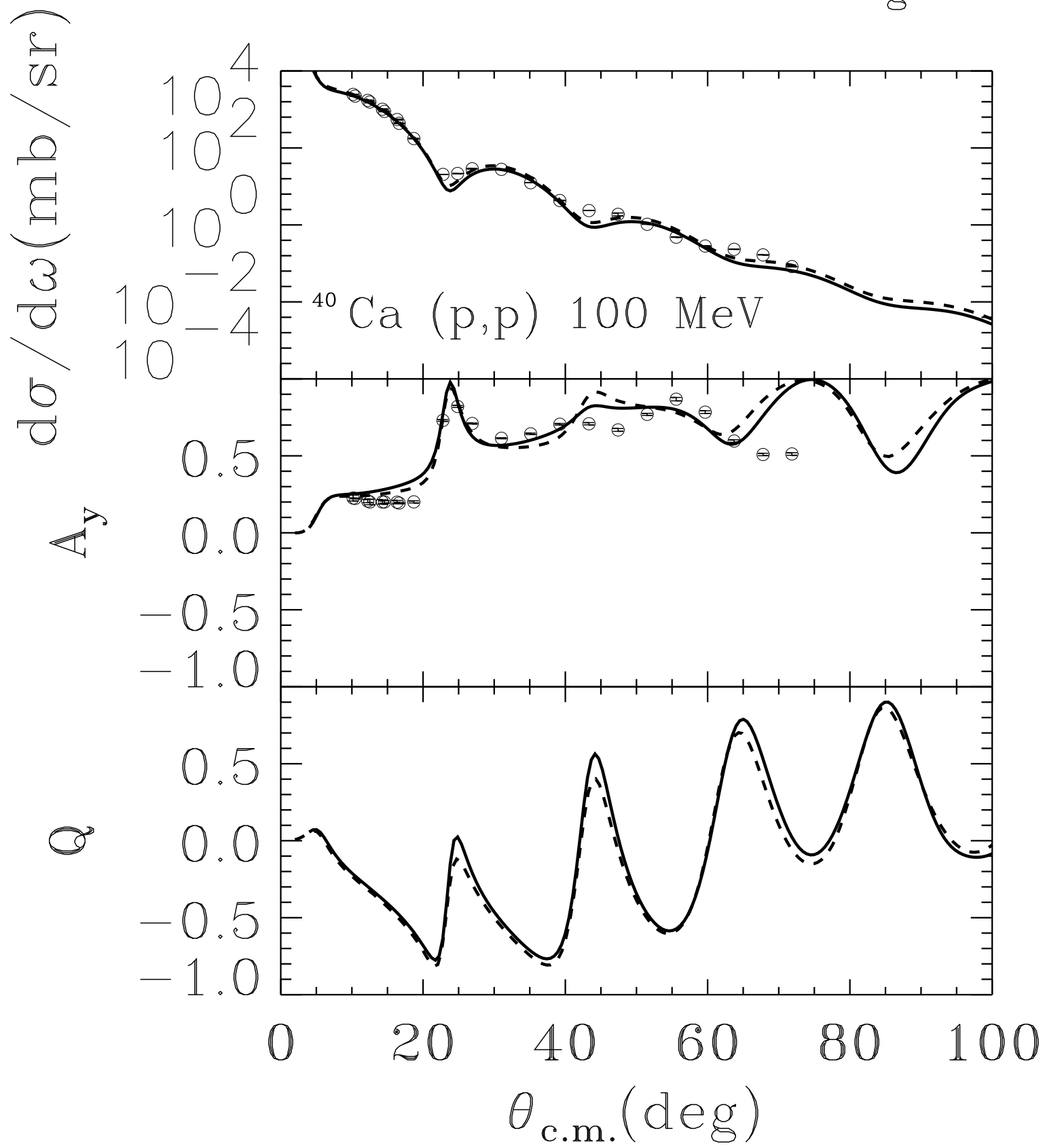


Fig. 9

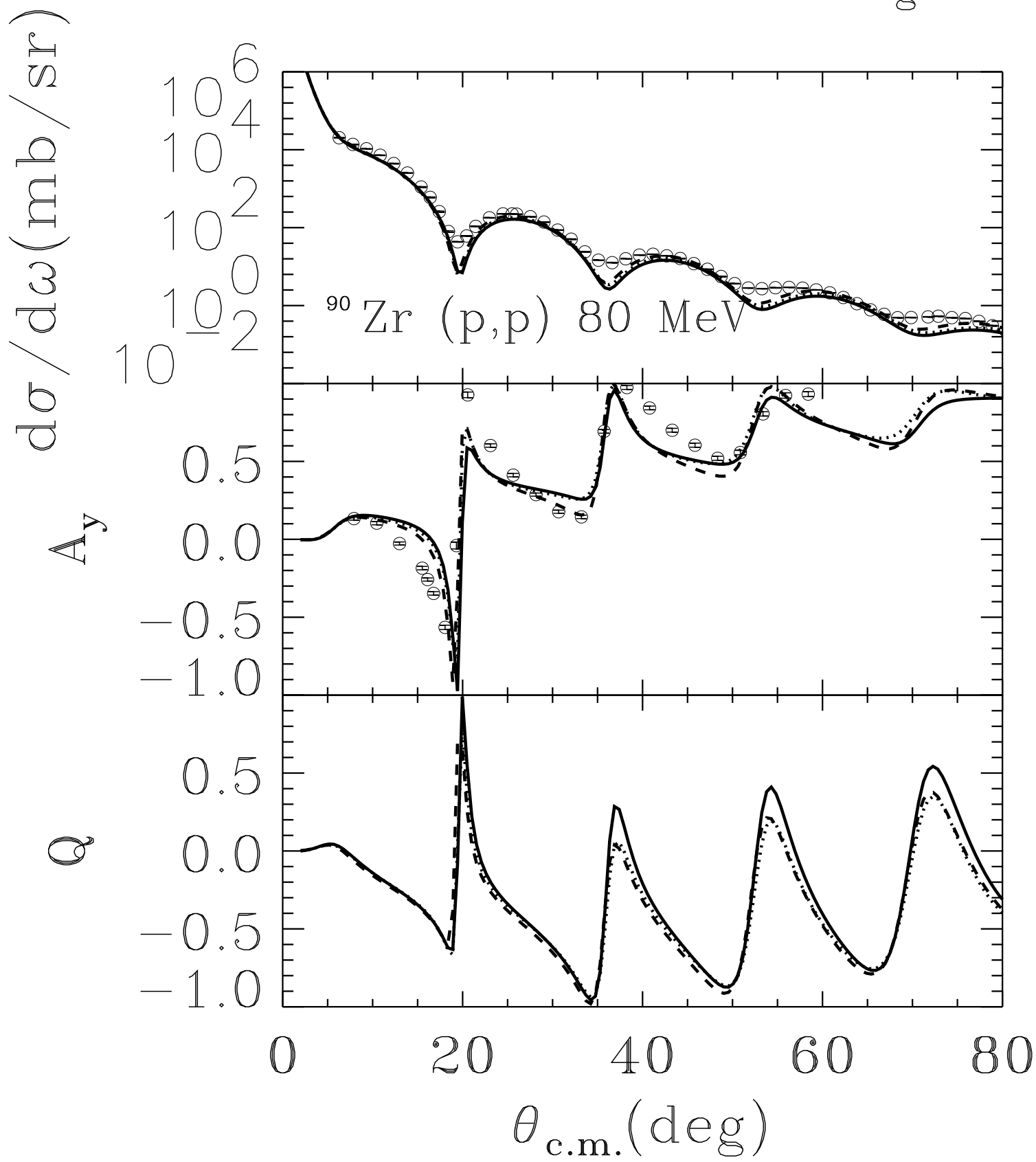


Fig. 10

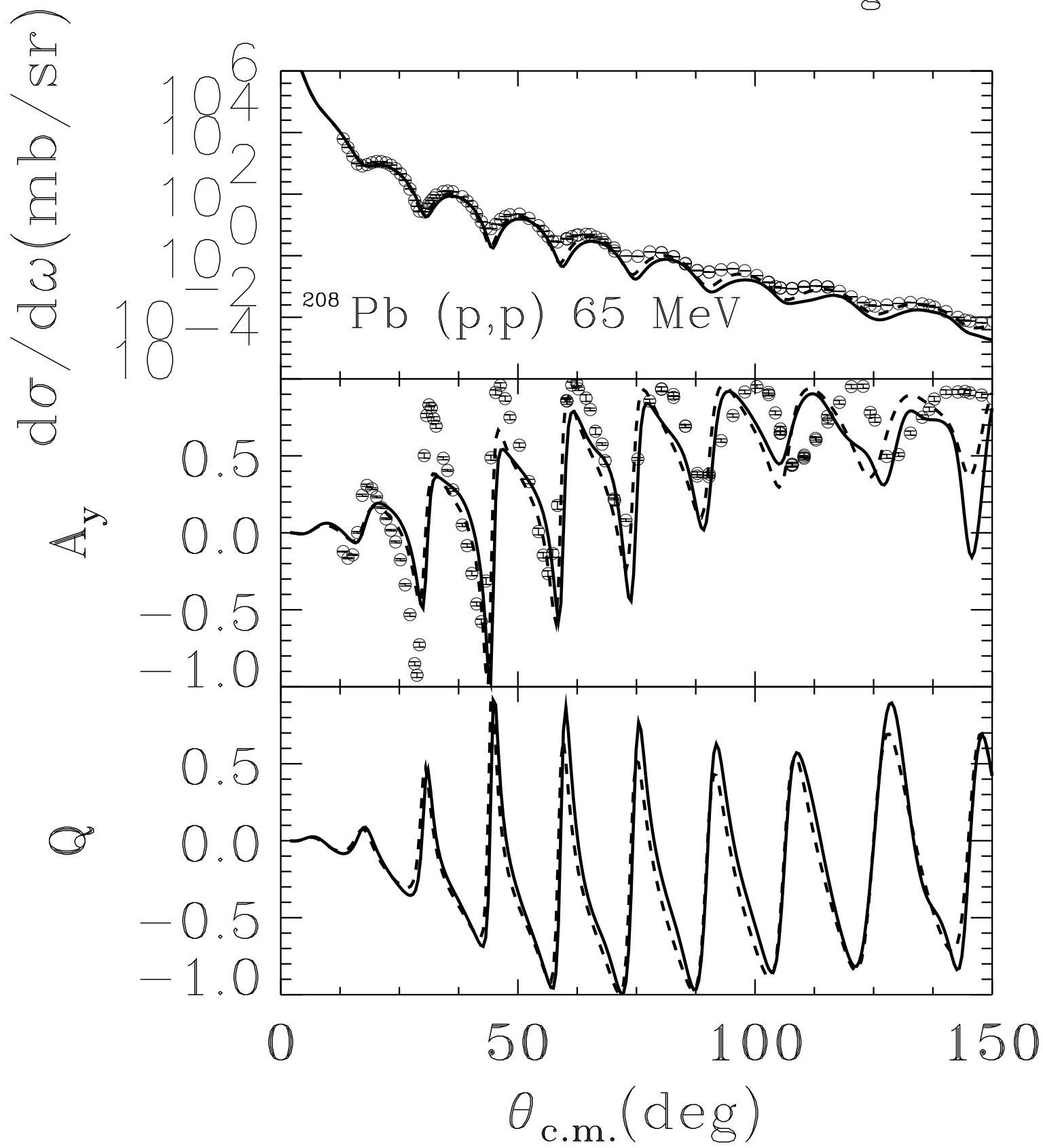


Fig. 11

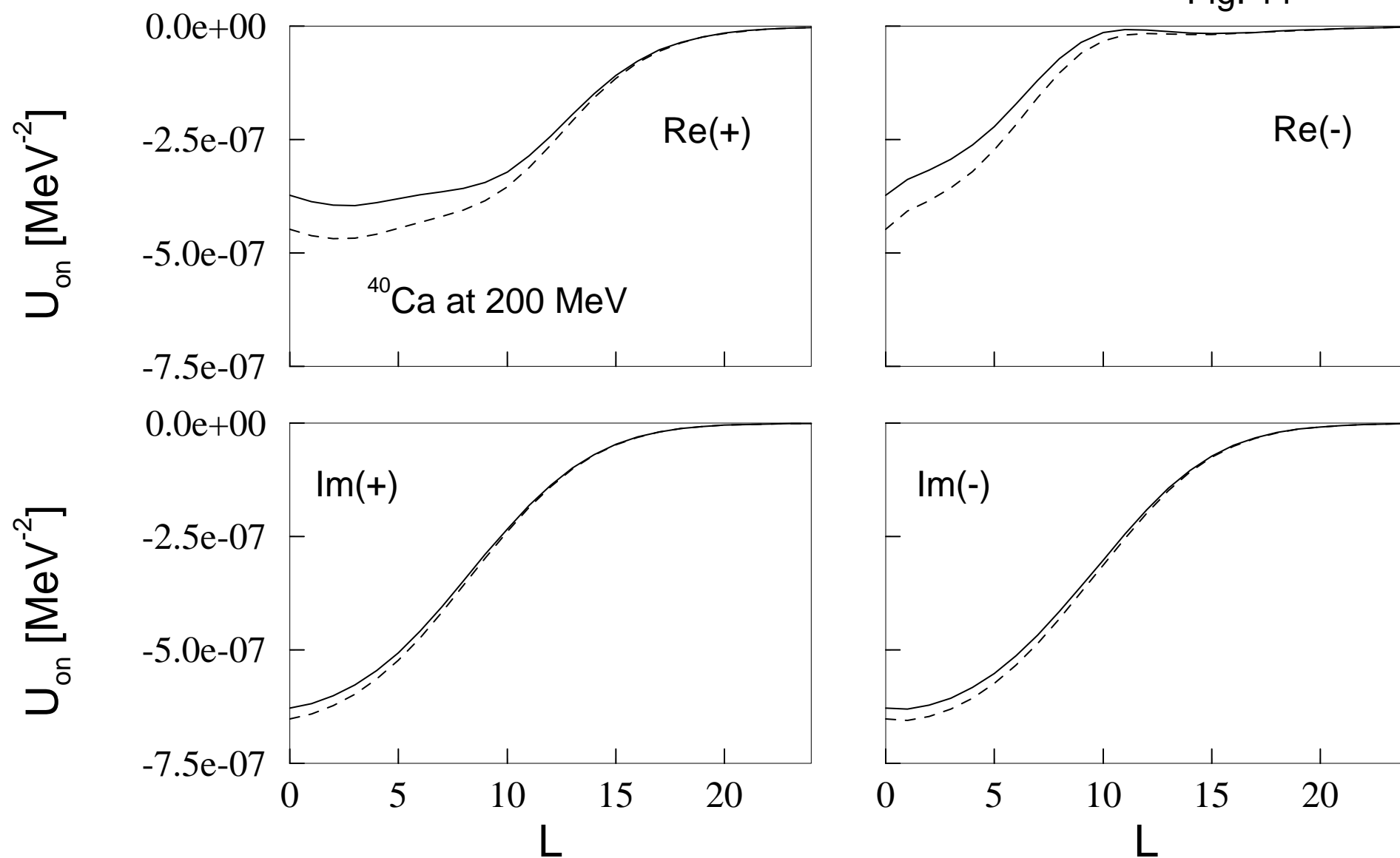




Fig. 12

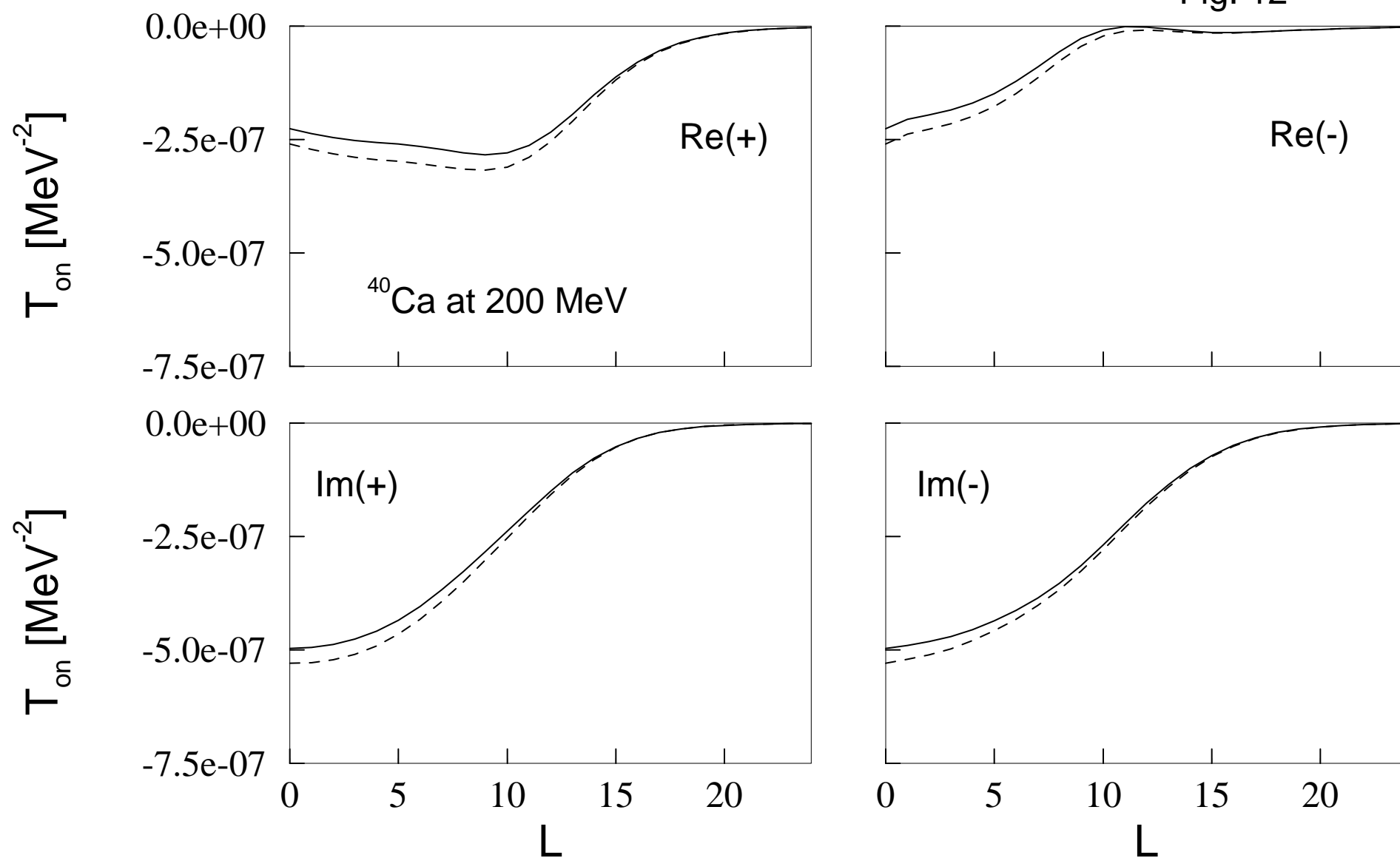


Fig. 13

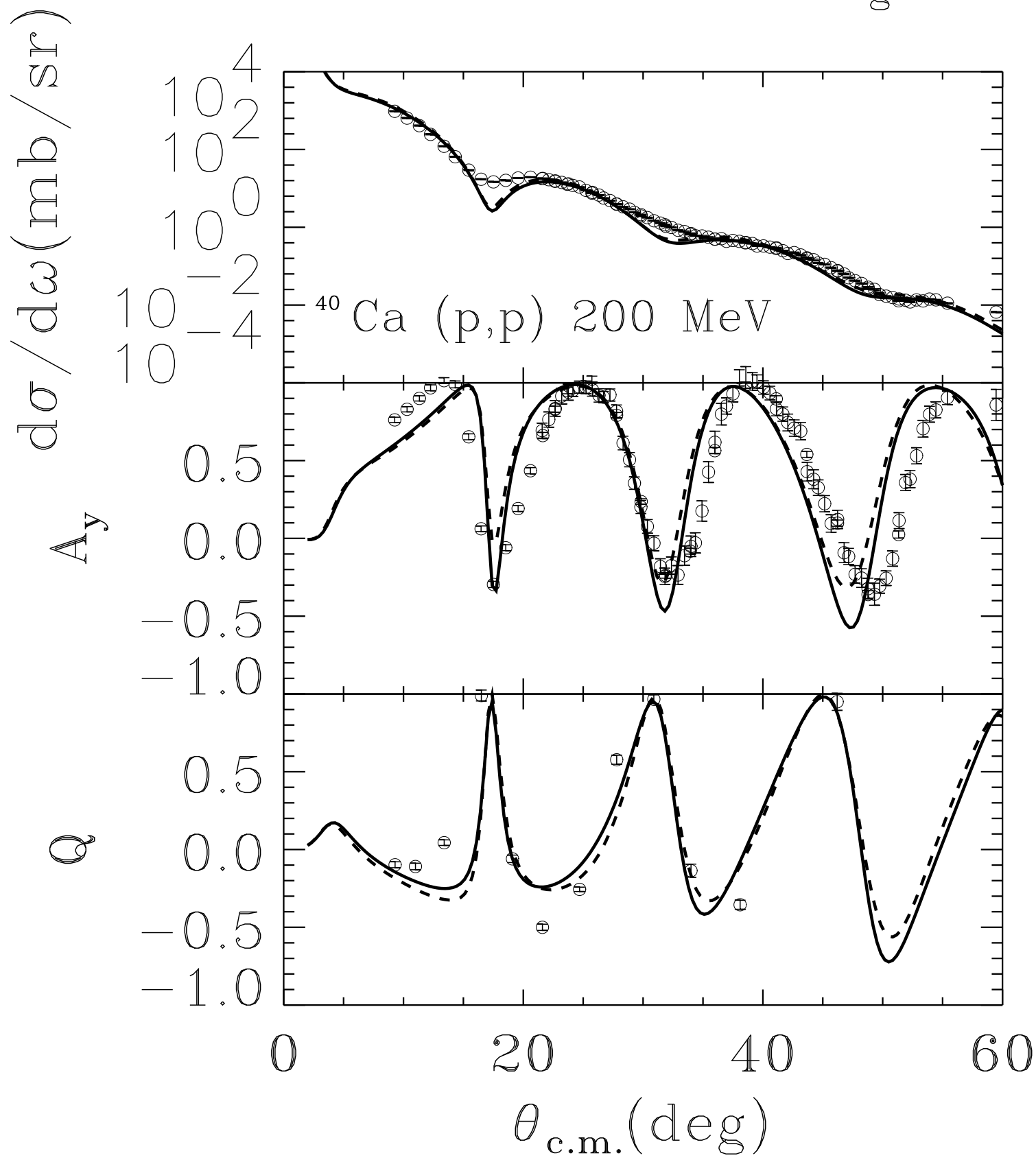


Fig. 14

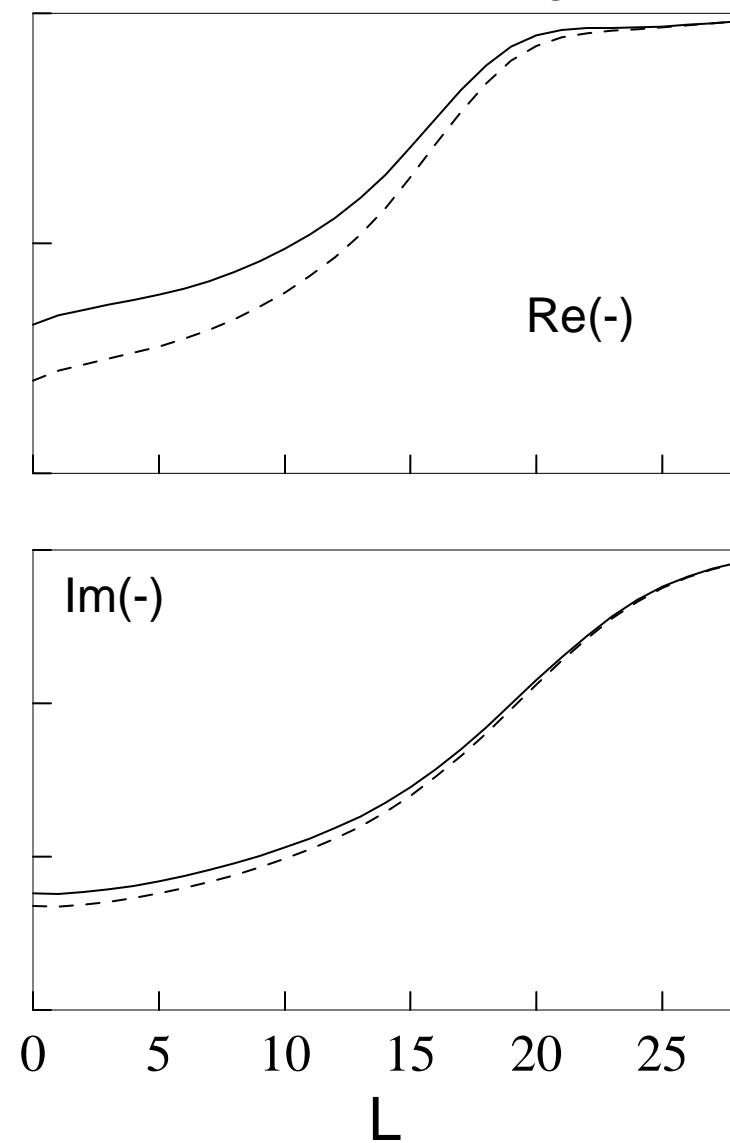
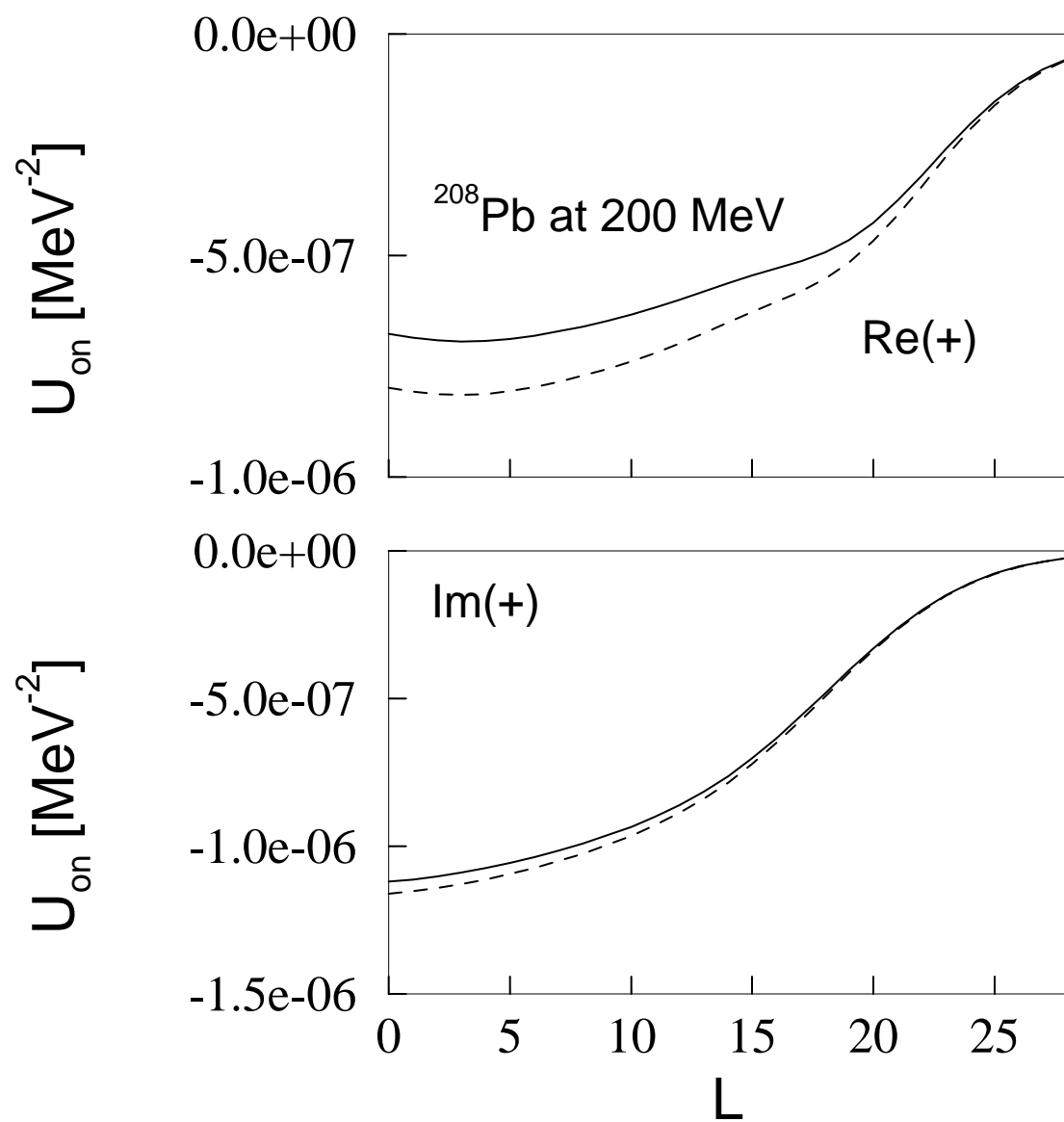


Fig. 15

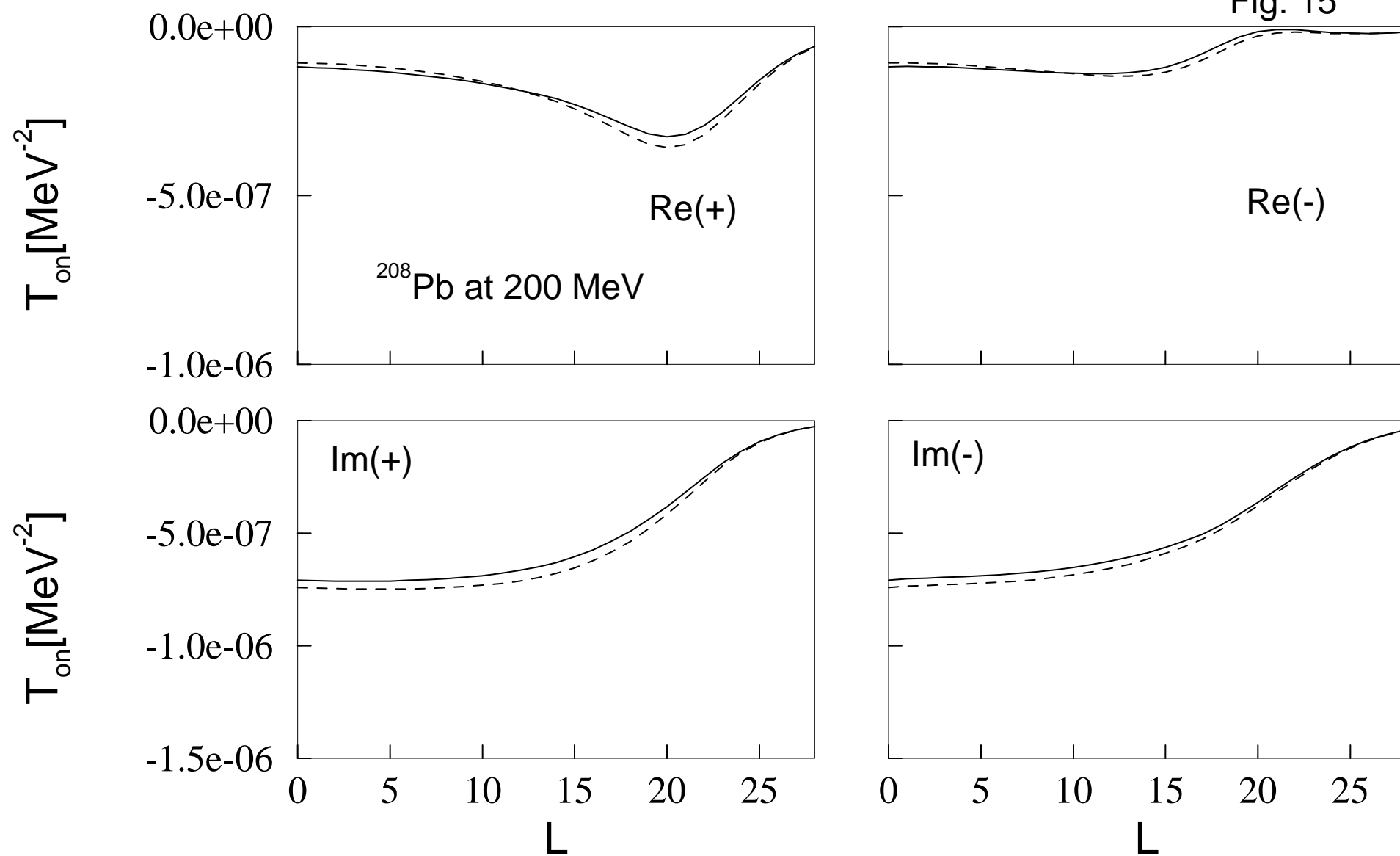
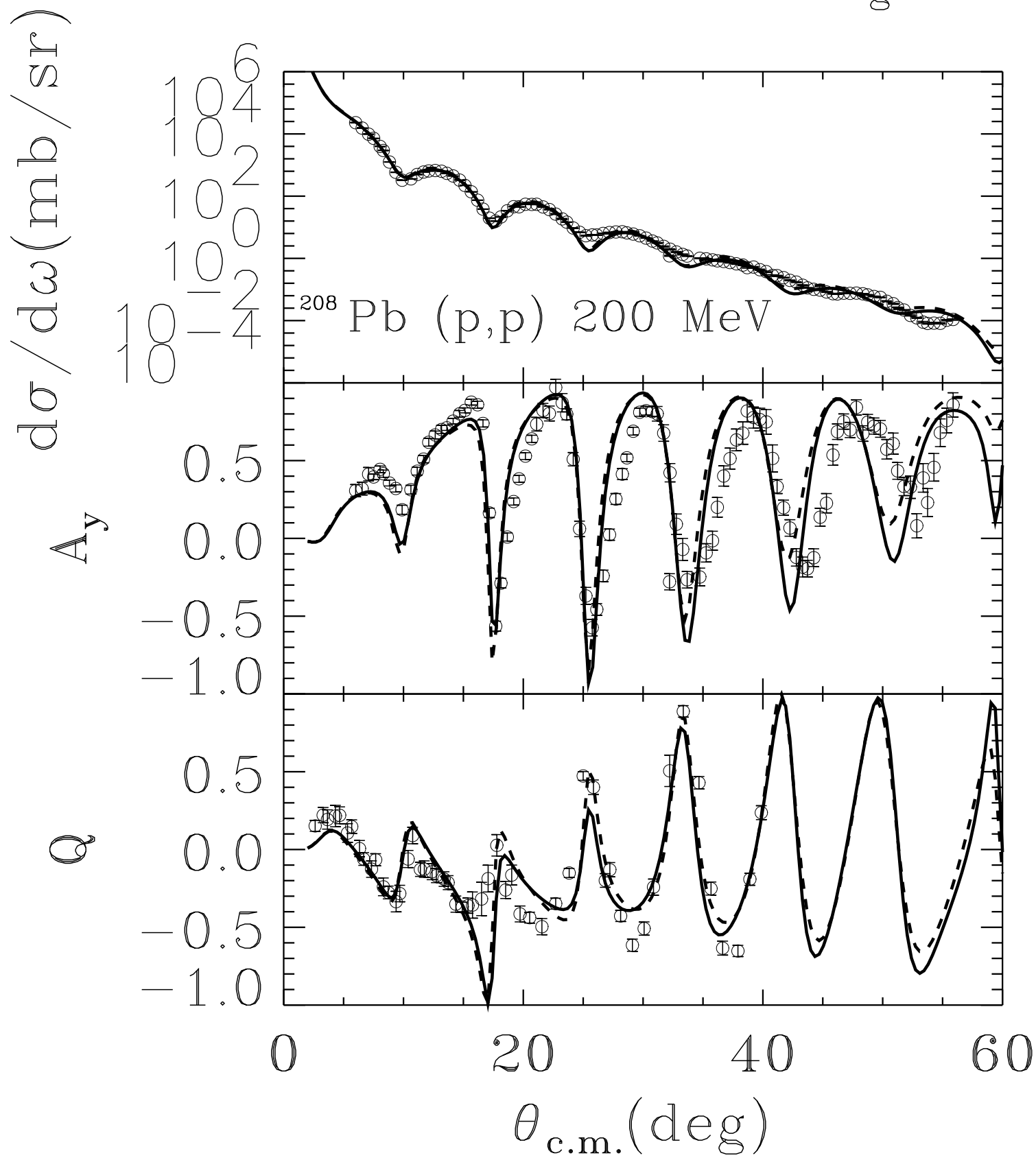


Fig. 16



**Fig. 17**

